CARRIE GALLIGAN

Catalytic Cracking of Jet Propellant-10
For Pulse Detonation Engine Applications

Mémoire présenté
à la Faculté des études supérieures de l'Université Laval
dans le cadre du programme de maîtrise en génie chimique
pour l'obtention du grade de maître ès sciences (M.Sc.)

FACULTÉ DES SCIENCES ET DE GÉNIE
UNIVERSITÉ LAVAL
QUÉBEC

mars 2005

Résumé

Le carburant hydrocarbure JP-10 est étudié comme agent propulsif destiné aux moteurs à détonation ainsi qu'à d'autres applications concernant les vols à vitesses élevées. La précraquage catalytique du JP-10 pourrait produire un mélange d'oléfines légères plus facile à détoner. Un mélange d'hydrocarbures aliphatiques, pour la plupart légers, présente l'avantage d'être moins enclin à la carbonisation que des mélanges comportant de fortes teneurs en hydrocarbures aromatiques. Cette réaction endothermique de précraquage offre le même potentiel que celui d'un puits de chaleur trouvé dans des applications de vols à vitesses élevées pour lesquelles toute hausse de la masse du système de refroidissement contrevient à une plus grande efficacité du moteur. Plusieurs essais de craquage catalytique hétérogène furent réalisés à l'aide d'un réacteur tubulaire et les gaz produits analysés par GC/MS et par GC. Deux formes de zéolithe nanocristalline (n) ZSM-5(24h) et nZSM-5 (6h) et trois formes de silico-aluminophosphate SAPO-5A, SAPO-5B et SAPO-11 furent testées. SAPO-5 et nZSM-5(24h) apparaissent être les candidats les plus propices au précraquage du JP-10. Ces dernières ont permis de convertir plus de 90 % de JP-10 en un mélange d'hydrocarbures principalement composé de molécules en C_4 et moins (C_3 à C_1). nZSM-5(24h) ont procuré le plus petit rapport de masse de carbone, CR ($C_5{}^+$:$C_4{}^-$), à des températures situées entre 350 °C et 450 °C et le taux de conversion le plus élevé à des températures supérieures à 500 °C. SAPO-5A & B ont présenté le taux de conversion le plus élevé mais le plus petit CR entre 400 °C et 500 °C.

Abstract

The hydrocarbon jet-fuel, JP-10, is being studied as a possible propellant for the Pulse Detonation Engine (PDE) and other high-speed flight applications. Catalytic pre-cracking of JP-10 could provide a more easily detonated mixture of light olefin products. A mixture of mostly light hydrocarbons has the added benefit of being less prone to coking than a product mixture heavy in aromatics. This endothermic reaction also offers potential as a heat sink in high-speed flight applications where the extra weight of an onboard cooling system would hinder engine efficiency. Several heterogeneous catalytic cracking tests have been done using a Bench Top Tubular Reactor and the products were analyzed with GC/MS and GC. Two forms of nanocrystalline zeolites, nZSM-5(24h) and nZSM-5(6h), and three forms of silico-alumino-phosphates, SAPO-5A, SAPO-5B, and SAPO-11 successfully catalyzed the cracking of JP-10; however, SAPO-5 and nZSM-5(24h) have proven to be the most promising catalyts. Both catalysts converted over 90 % of JP-10 ($\sim$ 3s residence time) into a mixture of hydrocarbon products consisting mainly of C_4 and lower chain hydrocarbons (C_3 to C_1). nZSM-5(24h) demonstrated the lowest carbon mass ratio, CR ($C_5{}^+$:$C_4{}^-$), between 350 °C and 450 °C and the highest conversion rates above 500 °C. SAPO-5A & B demonstrated the highest conversion rates and the lowest CR between 400 °C and 500 °C.

Preface

First and foremost I must thank Eric Fournier, Rob Stowe and my co-director Prof. Charles Dubois for giving me the chance to advance my education. Without their support and encouragement this project would not have been possible. As my co-director Prof. Charles Dubois was always there when I needed a little motivation or direction in achieving my research objectives. I would also like to thank the other members of the Precision Weapons section, especially Paul Harris, Sophie Ringuette, and Rocco Farinaccio who were always willing to help and lend advice.

During this project, I was very lucky to work with many wonderful people at Laval University. I would like to thank everyone in Prof. Kaliaguine's research team who were always willing to lend technical assistance, especially Gilles Lemay. However, this work would not have been successful without the advice and innovative ideas from Dr. M. Hassan Zahedi-Niaki. I cannot thank him enough for his constant patience and assistance.

Finally, I must thank my director Dr. Serge Kaliaguine who was available to give advice and his thorough corrections has led to a work that I can be proud of.

The funding provided by the Department of National Defense greatly aided me in achieving this goal. I am grateful for having this opportunity to share my research with the scientific community and grow as a scientific researcher.

To all my loved ones who kept me confident and motivated throughout the years.

Contents

List of Figures

List of Tables

Chapter 1

Introduction

Since the mid 1980s there has been a renewed interest in pulse detonation technology. The desire for a long-range, high-speed, air-breathing propulsion missile has been the primary objective behind recent pulse detonation engine (PDE) research. However, PDEs have also been found suitable for other flight systems, such as lightweight, low-cost space transportation and long-range Unmanned Air Vehicles (UAV)[1]. The PDE is a transient, detonation-based technology that operates on the principle of cyclical filling and detonation of a fuel-oxidizer mixture in a combustion chamber. In theory, the PDE could be two times more efficient than popular combustion engines if the propellant could detonate within specified parameters by a low energy igniter.

There are still many challenges to be met before a practical PDE system is developed. The challenge facing the current study involves the fuel and the ignition system. The study of liquid hydrocarbon propellants plays an integral part in the development of supersonic and hypersonic air-breathing flight systems. To date there has been little success operating a PDE using a conventional fuel. Operating engines with rare, easily detonated fuels, such as hydrogen, would lead to high operating costs and lead to other concerns, such as safety. The hydrocarbon jet fuel, JP-10 is being specifically targeted as a fuel in a PDE for its high thermal stability and density properties, low cost, and widespread availability. Logistically speaking, JP-10 is a perfect fuel to be used in a PDE; however, it has been realized that there will be major problems with detonation timings to overcome[2].

The major consequence of using a very stable fuel like JP-10 is the difficulty to initiate a detonation by using a low-energy ignition source. Catalytic pre-cracking has been suggested as a means to reduce the critical energy of heavy hydrocarbons by forming a mixture of light hydrocarbon products that would therefore reduce the power needed to activate a detonation. A more easily initiated, mixture of C_4 and lower hydrocarbon products could be obtained from the large molecule based JP-10, at appreciably low operational temperatures and pressures by way of a heterogeneous catalytic reaction. Hydrocarbon cracking also offers the added benefit of having large

endothermic heats of decomposition, which could be exploited for cooling by using heat absorbed from the engine to continue the decomposition reaction. A simple catalytic tube-reactor could be used during acceleration and essentially, turned off at cruise speed when the maximum cooling ability of the fuel is required. This would eliminate the need for an additional heat source for take-off or at lower flight speeds[3]. Catalytic pre-cracking also offers enhanced selectivity for light olefin products giving the added benefit of reduced amounts of undesired products, such as aromatics. Aromatics are known to augment soot formation and increase radiative heat of the combustor line[4].

The objective of this study is to identify the most suitable cracking catalyst(s) to create a stable mixture of light hydrocarbons, preferrably light olefins with a reduced initiation energy in order for JP-10 to be a viable fuel in a PDE. With a strong knowledge base of the products produced from cracking JP-10 with various catalysts it would be possible to design a chemical reactor to be used in a PDE fuel injection system. A small reactor that requires little or no alternate energy source would be a simple method to pre-crack JP-10 and introduce the light hydrocarbon product mixture directly to the ignitors. The most suitable catalyst(s) will ideally have a high selectivity for C_2, C_3, and C_4 olefin products, favouring lower temperature ranges (between 250 and 500 ^oC). By meeting these objectives, it may be possible to construct a reasonably sized PDE that would be fuelled with JP-10 and possibly, other common hydrocarbon jet fuels, such as Quadricyclane and RP-1. A PDE would improve long distance travel at supersonic speeds, which will not only be useful for military applications but could also be the answer to low cost, sub-orbital flight.

Chapter 2

Literature Review

2.1 Important Concepts

2.1.1 Steady versus Unsteady state Engines

An air-breathing engine is classified as either steady or unsteady state. The most common is the steady state combustion process (or quasi-steady state), where burning occurs by deflagration[5]. These engines are constrained to constant pressure created by heat addition, and as a result, have limited efficiency[5]. Some popular types of continuous combustion engines include gas turbines and turbojets[5]. Less frequently seen types of engines are based on intermittent combustion, governed by the fuel-air flame speed and combustion chamber shape and size characteristics[5, 6]. Unsteady propulsion systems are rather simple devices that can be based on deflagration, such as the pulse jet, or detonation, such as the PDE[6].

2.1.2 Deflagration versus Detonation

Deflagration and detonation are two types of combustion; the latter being the most common as it is less energetic and easier to control. The most distinct difference between deflagration and detonation is the flame speed. A deflagration reaction propagates at relatively low flame speeds, because it is dependent on the diffusion reaction rate of the unburned gases in front of a flame and on the burned gases behind the flame[5, 6]. Deflagration flame speeds are in the order of **one or more meters per second** for most typical hydrocarbon/air mixtures[6]. The most readily observed deflagrations produce small decreases in pressure and therefore, can be modeled as a nearly isobaric (or constant pressure) process[5, 6].

On the other hand, detonation is a much more energetic phenomenon than deflagration. It is a supersonic combustion that typically propagates at a **few thousand**

meters per second relative to the unburned fuel-air mixture[6]. Detonations can be described as supersonic shock waves that initiate and are closely coupled with a thin flame front (the combustion region)[6]. The detonation wave (or shock wave) compresses the fuel-air mixture, which acts like a fluid. This increases pressure and density, in addition to the already increasing temperature. Due to the high-speed nature of a detonation wave, a detonation can be modelled as a constant volume combustion process[6].

2.2 Pulse Jets

It is worthy to note the difference between the more commonly understood pulsejet concept and pulse detonation. Pulsejets were the first intermittent combustion jet engines ever developed for large-scale use[6] and provided a base for PDE technology. One of the earliest and most notable pulsejet powered devices was the German V-1 "Buzz Bomb" used in World War II[4-6]. The basic design is shown in Figure 2.1[1]. At present, the pulsejet is only commonly used for jet engine and rocket models.
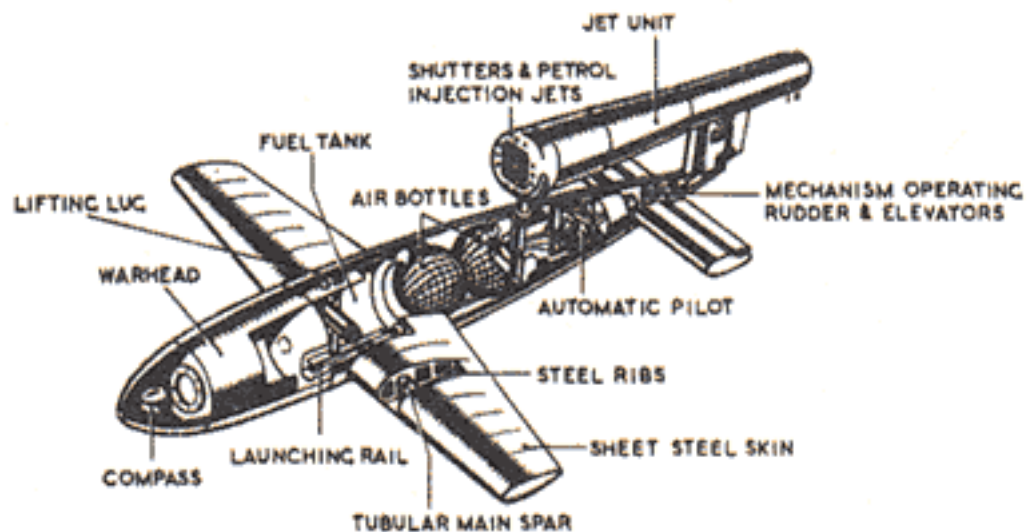
Figure 2.1 World War II German V-1 Buzz Bomb

The operation of a pulsejet is based on repetitive combustion ignitions using a spark plug. A simple explanation of how a pulsejet engine works is given in Figure 2.2. When opened, mechanical reed valves draw fresh air into the combustion chamber.

---

[1]Provided by http://www.eugeneleeslover.com/USNAVY/CHAPTER-11-D.html, a GNU free documentation website source.

Opening timings for the valves are based on the acoustical frequency of the combustion chamber. The combustion chamber consists of a central ignition region joined to an exhaust duct[7]. The major disadvantage of a pulsejet is it provides only a narrow range of thrust level variation, because the operating parameters are fixed with the size of the engine. The entire internal engine geometry would have to be changed just to increase or decrease the thrust[7].
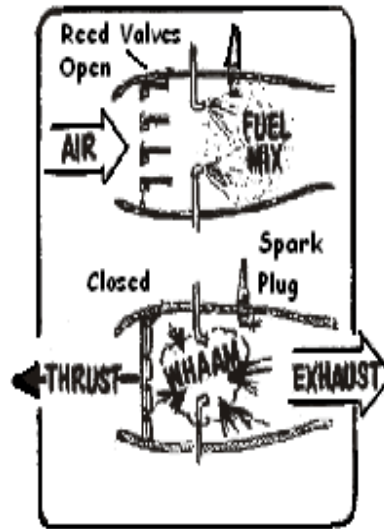
Figure 2.2 How a pulsejet engine works

The performance of pulsejets is defined by the properties of deflagration waves. Low deflagration flame speeds limit the maximum pressure in the combustor chamber and engine operating frequency that can be achieved. As a consequence, the performance of pulsejets is unpromising compared to steady state devices, such as turbojets and ramjets[2].

---

[2]William Avery first designed a ramjet following the same basic principle of a jet engine (ie. intake, compression, combustion, exhaust). When air enters any jet engine, its speed decreases and its pressure increases, which is called the ram compression effect. At high speeds this process can be fairly effective and can compress enough oxygen to efficiently burn the fuel for the engine. Typically, ramjets do not work effectively until the airspeed exceeds 1000 km/h and they do not outperform traditional jet engine designs until supersonic speeds. Like PDEs, ramjets reduce engine complexity by eliminating most of the moving parts, such as the compression fans in the front of the engine. A wide flight envelope or range of flight conditions, such as low to high speeds and/or low to high altitudes, can force significant design compromises.

Ramjets are built to utilize the compression effect through a careful inlet design. Beyond that the engine is largely nothing more than a well-designed tube, rendering it particularly useful in applications requiring a small and simple engine for high speed use. Therefore, ramjets are almost exclusively used in missile applications, where they are boosted to operating

It was assumed that the pulsejet combustion process was similar to the steady-state Lenoir constant-volume cycle, meaning the frequency of the combustion pulsations could be predicted by means of steady-state acoustical wave motion. However, the efficiency of the pulsejet, as determined experimentally, was much lower than a constant-volume process[7]. Studies have now shown that early pulsejets operated on an approximately constant pressure cycle, which is known to have lower combustion efficiency than the constant volume cycle[7].

2.3 Pulse Detonation Engine

By replacing a constant burning fuel, as in a ramjet or rocket, it is possible to use impulses created by sequential detonations as thrust. These impulses are very rapid explosions that can propagate over 2000 m/s. In principle, detonations are an extremely efficient means of combusting a fuel-oxidizer mixture and releasing its chemical energy content[8]. The high flame speed of detonation combustion provides stronger evidence that it occurs as a constant volume process, unlike as found with the pulsejet, where its unsteady state deflagration combustion actually is a constant pressure process[6]. Bussing et al.[6] theoretically determined that depending on the compression ratio, an engine that uses detonation in place of constant burning could be 30 % to 50 % more fuel-efficient assuming the same propulsive efficiency could be maintained.

In addition to fuel efficiency, it has been proposed that a PDE could also provide advantages of lower weight and cost when compared to existing gas turbine engines. Unlike complicated turbine engine designs, in its simplest configuration, a PDE is just a long detonation tube closed at one end with few moving parts. As depicted in Figure 2.3, the PDE operates on the principles of cyclical filling and detonation. The tube is filled with an air-fuel mixture that is ignited at the closed end of the tube and detonates within the constraints of the tube dimensions. This initiates a detonation wave that propagates at supersonic speed until it exits the tube. The tube is purged of the combustion products and a new mixture of air and fuel is injected, repeating the cycle. This simple unsteady state combustion process eliminates the need for pumps, turbines or even compressors[9].

The theory behind a PDE is simple, but the technology is not. Although there is potential applications spanning the entire flight envelope including subsonic, supersonic, and hypersonic flight, there are still many unresolved issues concerning the PDE. Fuel-air mixing, detonable mixture injection, reliable thrust measurements, characterization of cycle loss, and efficient detonation initiation are only some examples of areas that need to be researched before a practical and affordable PDE can be realized[8].

---

speeds by a rocket motor, or by being attached to another aircraft (typically a fighter). Today, ramjets have generally been replaced by small turbofans or rockets, because the speed cannot be changed during flight[6].

Basic Principles of Operation

1. Filling of an air-fuel mixture; ready for detonation.

2. Initiation and propagation of the detonation.

3. Loading of the tube by expansion waves.

4. Injection of the mixture and beginning of a new cycle.
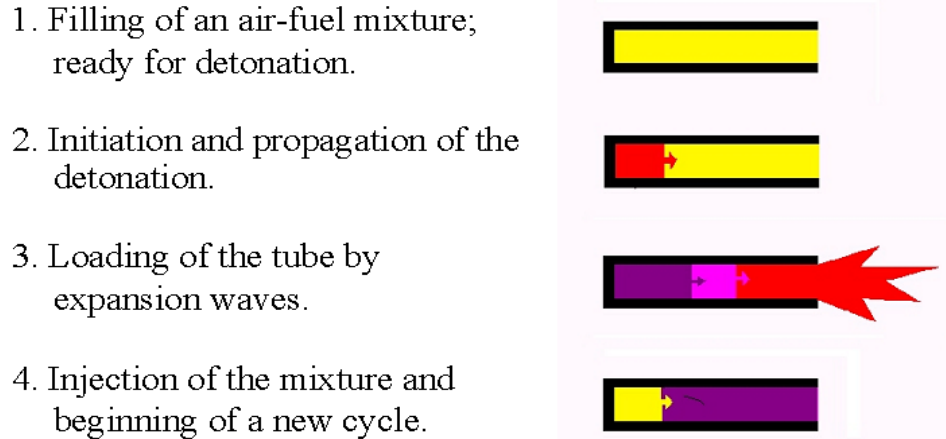
Figure 2.3 Basic operation of a Pulse Detonation Engine

2.4   Difficulty with PDE Fuels

Implementation of a PDE into a practical system requires improved knowledge in many areas of pulse-detonation phenomena. The area of concern of this research project is the time to detonation of the chosen propellant, a common hydrocarbon jet propellant, called JP-10 ($C_{10}H_{16}$). The majority of studies on PDE have been based on gaseous systems, such as hydrogen, acetylene, and ethylene. Owing to the lower boiling points and low critical energies, these light gaseous fuels have shorter ignition times and lower combustion temperatures. This eliminates the need for high-energy ignition systems and heated test facilities. However, gaseous fuels pose severe explosion hazards, have large-scale storability problems, and are expensive and difficult to obtain, rendering them impractical to be used in actual flight systems. For these reasons, liquid or solid fuels are preferable.

The study of liquid hydrocarbon propellants plays an integral part in the development of supersonic and hypersonic air-breathing flight systems. The hydrocarbon jet fuel, JP-10 has been specifically targeted because of its high thermal stability and density properties, cost, and availability. Thermal stability is often characterized by the amount of deposits that a particular fuel forms at a specific temperature in a test device. By definition, a thermally stable fuel would create fewer deposits in the fuel system than an unstable fuel in a flight system[3]. Considering JP-10 is a strained-cyclic molecule, it is expected to act as other strained cyclic high energy density materials (HEDMs). For example, Quadricyclane, a strained ring compound that has density properties similar to JP-10, is highly unstable and significantly decomposes by 200 ^{o}C

in an oxygen free environment. However, JP-10 is a single di-cyclo molecule with a bridged carbon that demonstrates unusually high thermal stability. Experiments have demonstrated that even at 600 ^{o}C ($\sim$ 3s residence time), JP-10 only degrades by about 20 %[10].

The thermal stability of JP-10 is only comparable to the conventional rocket fuel, RP-1. There are two benefits from a chemistry point of view to using JP-10 over RP-1: JP-10 has a higher density, 0.94 g/cm^3 versus 0.81 g/cm^3, and JP-10 is a single molecule rather then a mixture of paraffins and cycloparaffins. The decomposition of a single molecule is more simple to analyze and control than a mixture of hydrocarbon molecules.

A major advantage for using hydrocarbon fuels is for their endothermic reaction properties. Supersonic and hypersonic vehicles will face severe thermal environments, particularly in the engine. For example, at Mach 8 a combustor surface that is not cooled will surpass 3000 K, which far exceeds known structural material capability. The thermal decomposition reactions of hydrocarbon fuels feature a substantial activation energy barrier and hence, offer a potential heat sink. Moreover, the resulting heat-of-combustion of decomposition products remain essentially unchanged or slightly increased. These heat-absorbing chemical reactions are supported by the energy extracted from heated air (ie. aerodynamically heated inlet air or compressor bleed)[3]. Gaseous fuels, such as hydrogen, do not offer the same heat capacity as hydrocarbon fuels, because they do not undergo thermal decomposition. Low density, gaseous fuels also require a large onboard storage capacity. By using high-density liquid fuels, the size of the vehicle can be decreased, thereby increasing engine efficiency.

A key development in making the PDE viable would be demonstrating the rapid formation of the detonation wave in a spark-ignited combustor, fueled with a conventional storable hydrocarbon[11]. A study published by the Naval Postgraduate School, investigated the detonability of JP-10[12]. One main conclusion of this preliminary work was that the detonation properties of this fuel, when mixed with air, were not sufficient to ensure the design of a PDE motor within an acceptable tube length. A practical PDE design that maintains the primary interest of developing a lightweight space vehicle has been suggested to have a maximum detonation tube length of approximately 1 meter. For JP-10 to be a practical option as a propellant in a PDE, its detonability properties must be enhanced by reducing its critical energy of initiation. This would ensure a shorter run-up distance for deflagration to detonation transition (DDT) to achieve the proposed optimal design of a shorter tube length in a PDE.

DDT is a widely used method to study changes in the detonability properties of an energetic material. A detonation wave can easily be initiated in a test shock tube by igniting an explosive gaseous mixture at one end, which produces an accelerating flame-front that propogates towards the other. The ability of the deflagration to accelerate and transit to a detonation depends on the parameters that determine sufficiently high burning rates. Burning rates are determined by how rapid the hot combustion products,

active free radicals (produced through various reaction mechanisms) and unreacted gas mix[13]. The pre-detonation distance, or run-up distance, travelled by the accelerating flame before transition, also depends on how fast the mixture readily generates these free radicals. For this reason, the run-up distance to DDT represents an experimental measure of the sensitivity of a detonable mixture; the shorter the run-up distance, the more sensitive the mixture with respect to detonation[14].

2.5 Tried Methods of Implementing JP-10 into a PDE System

Many options are being tried on an international scale to advance JP-10 into a PDE system. The use of chemical additives, studying the so-called 'blue flame' phenomenon, and the use of obstructions and distributed igniters in a detonation tube are just some examples that have been studied in Canada. Despite the extensive research that has been done, a practical method to reduce the run-up distance for DDT of JP-10 has yet to be found. This leaves the use of thermal, heterogeneous catalytic cracking as the most promising solution to this detonation problem.

2.5.1 Chemical Additives

Diesel companies have been studying and using homogeneous catalysts or additives to enhance combustion properties of various common fuels for many years. Additives, usually organic nitrates, are well known to boost a fuel's ignition properties and hence, their performance in engines. Chemical additives could offer an inexpensive, flexible method to enhance the detonability properties of jet fuels. For example, the addition of 500 to 10,000 ppmv (0.05 % to 1 % by volume) 2-ethyl-hexyl-nitrate (2-EHN) has been shown to decrease the observed ignition delay of JP-7 and JP-8 by 16 % and 20 %, respectively[15]. However, Mikolaitis et al.[16] studied the ignition delay times of JP-10 blended with 10 % EHN, as well as other additives (10 % and 50 % methylated PCU alkene dimer, 10 % nitrobornane, and 10 % dinitronorbane) in air at pressures from 10 atm to 25 atm and temperatures from 1200 k to 2500 K using a shock tube. The study concluded that ignition delays were essentially insensitive to all of the additives tested. Pinard et al.[17] did achieve a shortened DDT run-up distance by adding roughly the same amount of pure oxygen as that that would be supplied by Nitrogen Oxide (NO_2)[17]. However, the study concluded that a chemical kinetic effect resulted from the reaction with NO_2 rather than with methyl radicals[17]. The disappointing results of these studies leaves few options left in respect to other possible detonation enhancing chemical additives.

2.5.2 'Cool Flame' Presensitization

A more promising JP-10 detonation enhancement method is the chemical presensitisation effect of the 'cool flame'. The 'cool flame' or 'blue flame' phenomena was first discovered in 1937 by Shtsholkin and Sokolik[18]. An important property of hydrocarbon fuels is their two-stage ignition mechanism. The first stage involves the partial oxidation of the fuel, which generates free radicals. When the concentration of free radicals reaches critical value they begin to decompose liberating a small amount of energy accompanied by light emission, the cool flame[12, 14]. Shtsholkin and Sokolik[18] suggested that a fuel may be presensitized by heating the fuel just before the cool flame temperature. Romano et al.[19] applied this theory to try to decrease the run-up distance to DDT of JP-10. A high-speed streak camera was used to capture the image of the cool flame. This cool flame study successfully demonstrated that the partial oxidation of a pentane-oxygen mixture via cool flame successfully reduces the run up distance of DDT by approximately 50 %.

By simulating cool flame kinetics and 'freezing' the chemistry, Landry et al.[19] performed sensitivity analyses, identifying that a combination of hydroperoxides and the elevated temperatures generated by the cool flame, play a major role in the ignition reaction mechanism. The addition of relatively small concentrations (~ 6 %) of tert-butyl hydroperoxide has a significant sensitizing effect (~ 50 %) on the detonation sensitivity of decane-oxygen mixtures at elevated temperatures. However, as was demonstrated with previous additive studies, the unique physical chemistry properties of JP-10 requires further investigation with peroxide additives specifically added to JP-10 before possible sensitization affects can be realized.

2.5.3 Mechanical Methods

In general, there are two ways to initiate a detonation: directly by using a high-energy source, or by a flame acceleration process, known as deflagration-to-detonation[20]. Sustained flame acceleration in a tube can lead to DDT, which is being studied as a possible detonation initiation scheme for PDEs. A conventional mechanical method for promoting flame acceleration in a tube to reduce the run-up distance of DDT is to place turbulence-generating obstacles, such as orifice plates, in the path of the flame. Under these boundary conditions the flame can accelerate to a velocity close to 1000 m/s. This flame acceleration is caused by the interaction of the flame with the turbulent flow of the unburned gas and the compression waves generated as a result of the expansion of the gas through the flame[21].

The initial stage of flame acceleration is characterized by flame area enhancement, commonly referred to as flame folding. Flame folding is caused by large-scale flow perturbations in the unburned gas generated by the orifice plates. At higher flame

velocities, small-scale turbulence generated in the shear layer downstream of each plate edge enhances the local burning velocity that promotes flame acceleration. Compression waves radiate ahead of the flame as it accelerates. These waves strengthen as they coalesce, eventually leading to the formation of a strong shock wave. Eventually, flame front instabilities, caused by reflected compression wave-flame interactions, become the dominant mechanism for flame acceleration. Ultimately, the flame chokes and reaches a maximum velocity corresponding to the speed of sound in the combustion products[21].
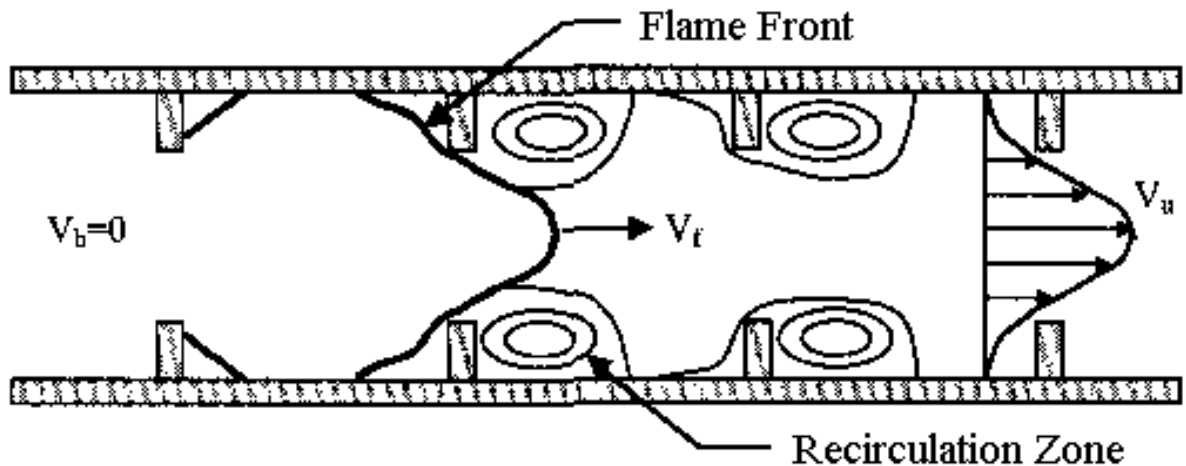
Figure 2.4 Recirculation zones in an obstacle laden detonation tube[20].

As shown schematically in Figure 2.4, the flow field in the unburned gas is dominated by recirculation zones behind each orifice plate. The core flow outside the recirculation zones is characterized by flow expansion between the orifice plates. This periodic flow expansion and contraction is responsible for the flame area enhancement, or flame folding. In an obstacle laden tube each plate is a source of perturbation to the flow ahead of the flame. Therefore, the frequency of this perturbation will impact how fast the flame accelerates. Based on experiments conducted with hydrogen using 3.1 m long and 15.2 cm diameter tube, the optimum obstacle spacing was found to be 1 tube diameter. However, flame acceleration was not observed in experiments using hydrocarbon fuel-air mixtures[20].

Another study using a 3.1 m long heated detonation tube with a 10 cm diameter completely filled with orifice plates equally spaced at one tube diameter was also conducted[21]. Experiments using JP-10/air mixtures performed at an initial pressure of 1 atm did not result in detonation initiation. There was also only a moderate enhancement observed in flame acceleration at the higher temperature of 573 K compared to the lower temperature of 373 K. This is consistent with the results found in other hydrocarbons tested and opposite to that observed in hydrogen. Intriguingly, detonation initiation was observed at all temperatures for tests performed at 2 atm[21].
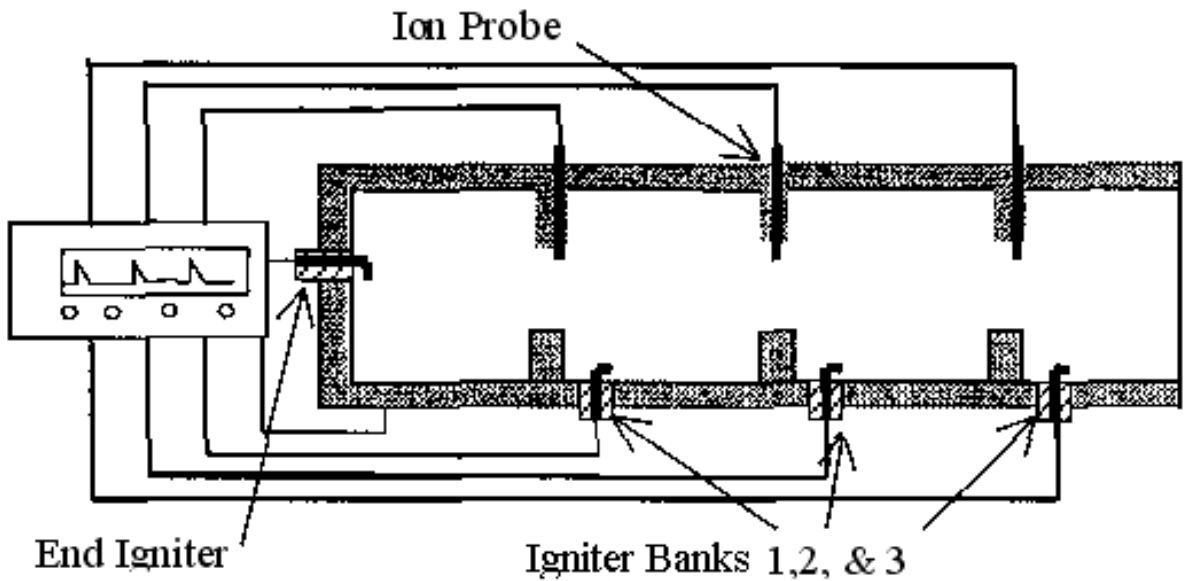
Figure 2.5 Igniter and obstacle laden detonation tube[20].

Stoichiometric[3] propane-air experiments were conducted using both an obstacle field (1 diameter spaced orifice plates) and a multi-point ignition system in a 3.05 m long tube with a 15.2 cm diameter[20]. It is important to note and will be further discussed later in this chapter, that previous experiments have shown that propane demonstrates similar detonation properties as JP-10. Even though JP-10 is the desired fuel for use in PDE applications it is more difficult to work with than propane since it requires preheating of the experimental apparatus to obtain a gaseous mixture[20]. As depicted in Figure 2.5, Four automotive spark plugs were placed behind each of the first six obstacles. The energy of each spark plug is slightly higher than that of a commercial automotive system ~ 250 mJ[20]. It was found that in the early stages of burning, before flame velocity reaches approximately 100 m/s, igniting a separate flame front ahead of the primary flame produced a higher flame velocity than that of the unaided flame acceleration. Two additional igniter banks were added, which heightened this effect up to a distance of 1.6 m. However, adding more than two igniter banks did not provide any further enhancement. Results also showed that multi-point ignition reduces the overall run-up time, which would allow for higher cyclic frequencies in a

---

[3]A fuel-air mixture is said to be stoichiometric when the combustion chemistry goes to completion. If there is insufficient oxygen present the combustion will be incomplete and the combustion products may contain unburned hydrocarbons and carbon monoxide. If too much oxidizer is present than required to produce a stoichiometric reaction the temperature of the reaction will be reduced. Under both fuel-rich and fuel-lean conditions the fuel-air mixture may reach a 'flammability' limit and the combustion reaction will not take place. This limit is also dependent on other parameters such as the size and energy of the ignition spark. Therefore, the engine performance is dependent on air-fuel equivalence ratios.

PDE[20].

However, this method does not reduce the large amount of power required to detonate JP-10. Therefore, despite the advancement of mechanical methods to improve DDT of heavy hydrocarbon fuels for a PDE, they are still the least desirable forms of detonation enhancement. Additional weight and friction are just two of the foreseen major problems for light-weight flight applications, such as long-distance missiles.

2.5.4 Catalytic Cracking

Due to the interest of specifically introducing JP-10 into a PDE, its detonation properties were studied by Austin and Shepherd[22]. Various nitrogen dilutions (fuel-oxygen to fuel-air) of vapour-phase JP-10 were tested in a detonation tube at 353 K. A high initiation energy and the large cell size characteristics of JP-10 mixtures indicated low mixture sensitivity to detonation initiation. Cell-size measurement is used as an implicit method to approximate a fuels ease of initiation. The cell-size of JP-10 is similar to that of propane suggesting propane could be used as a surrogate fuel to JP-10[22]. Nitrogen diluted mixtures of stoichiometric hexane-oxygen were studied as well, because cell widths for hexane-air and JP-10/air were also found to be comparable[22]. Schauer et al.[23] did achieve detonations in propane-air mixtures, but only over a small range of equivalence ratios.

Austin and Shepherd[22] furthered their research by studying the detonation properties of mixtures representative of the decomposition products of JP-10. The lower molecular weight fuel blends consisted of the addition of hydrogen, acetylene, ethylene, and carbon monoxide to hexane-air. The measured cell-size decreases, indicating increased sensitivity to detonation with increasing fraction of hydrogen, acetylene, and ethylene, in order of effectiveness[22]. The results of these studies suggest that pre-cracking JP-10 to lighter hydrocarbons could increase the detonation sensitivity by reducing its critical initiation energy. Therefore, the next logical step to be taken in the implementation of JP-10 as a fuel in a PDE is to use a catalyst to reduce JP-10 into a mixture of light hydrocarbon products.

Brabbs et al.[24] has shown that by reacting the fuel in a catalytic tube reactor the H:C ratio increases and the combustion temperature decreases, thus improving the fuels detonability. By using catalysis chemistry it may be possible to increase the cracking rate and control the reaction product ratios in order to produce a stable mixture of light hydrocarbons that would detonate within the desired detonation tube length.

The idea of using a catalytic reactor in a fuel injection system of a high-speed propulsion unit has already been well researched. An article published in Popular Science of November 2002 hinted that a catalytic converter is used in the fuel injection
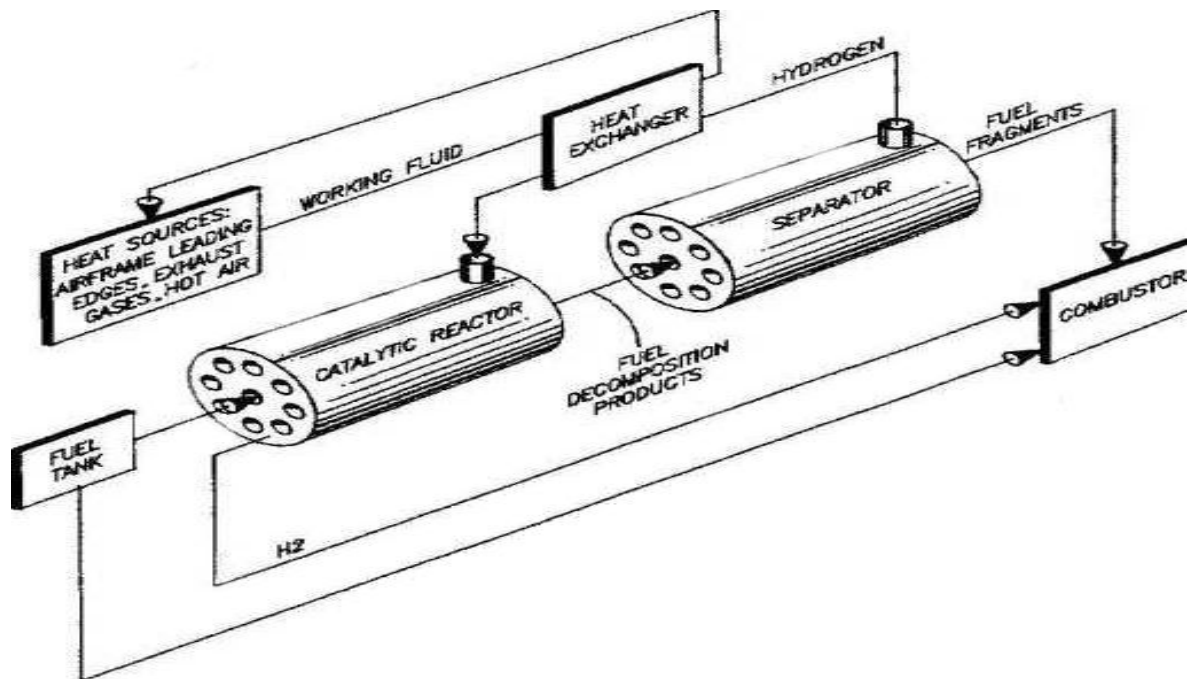
Figure 2.6 Catalytic reactor system with product separator[25].

system of a jet-fuel powered scramjet developed in a joint collaboration with NASA and the US Air Force[25][4].

An example of an already patented design of a catalytic converter to be used in detonation engine applications is depicted in Figure 2.6[25]. In this design catalytic pre-cracking is taken one step further by product separation, which takes better advantage of the light, more easily initiated hydrocarbon products. A stream of hydrocarbon fuel is catalytically decomposed to4.2 produce hydrogen and lower molecular weight fuel fragments that may be separated by molecular size. The hydrogen and lower molecular weight fuel fragments are introduced along with a stream of non-decomposed hydrocarbon fuel into the combustor of a high-speed propulsion unit. The method results in a wider combustor operating range, with higher combustion rates and increased flame stability, achieved through more rapid diffusional mixing. The process effectively extends the operating limits of gas turbines, and especially in ramjet and scramjet combustors[25].

Consequently, it is the chosen fuel that has become the main limiting factor in PDE engine design. An efficient cracking catalyst that produces the correct product selectivity must first be identified. To date, there has been little success at finding a low-cost, easily produced catalyst to crack JP-10. This research project explores some easily and inexpensively synthesized catalysts using a benchtop tube reactor to

---

[4]The Scramjet is an advanced version of a ramjet based on supersonic combustion[26].

determine the conversion rate of JP-10 to a lighter hydrocarbon mixture and attempts to identify the majority of these products.

2.6 Hydrocarbon Cracking

Hydrocarbon cracking (HC) involves the rupture of C-C molecular bonds creating lighter hydrocarbons from heavier hydrocarbons[27]. Cracking reactions are endothermic and thermodynamically favoured by high temperatures[27]. Pyrolysis or thermal cracking, catalytic cracking, and hydrocracking are the three methods of HC. Pyrolysis is carried out in the absence of oxygen and occurs at the highest temperatures ($\geq$ 1000 K). Catalytic cracking occurs at temperatures between 200 ^{o}C and 600 ^{o}C and pressures around 1 atm. As the name suggests, hydrocracking occurs in the presence of hydrogen at temperatures between 250 ^{o}C and 400 ^{o}C and under high pressures, typically between 80 atm and 200 atm. Hydrocracking is a complicated process that would require a hydrogen reserve and is therefore, not considered as a practical HC method for PDE applications.

2.6.1 Thermal Cracking versus Catalytic Cracking

Petroleum refining primarily involved thermal cracking before the discovery of catalysts[27]. Thermal cracking continues to have importance for converting naptha into light olefins and for visbreaking[5] of heavier feedstocks[27]. Thermal cracking usually involves a scission at a bond located β to the carbon atom having the unpaired electron and there is little transfer of the radical from one hydrocarbon chain to another. The unpaired electron cannot move from one carbon atom to another on the chain, inhibiting isomerization reactions[27]. For this reason, thermal cracking generally produces high yields of ethylene, low yields of methane, and low yields of evenly distributed α-olefins, which gives a high ratio of olefinic to paraffinic products[27]. There is also an absence of isomerized products because of the immobility of the unpaired electron.

Although thermal cracking of JP-10 would theoretically produce the ideal yield of gas products, it is limited by the need of high temperatures to achieve a high enough conversion to have any significant effect on the initiation energy. Thermal cracking experiments at a reactor temperature of 500 ^{o}C and liquid fuel flow rates between 2.3 g/hr and 10.6 g/hr yielded conversion ratios of approximately 3 % and less[28]. Decreasing the liquid fuel flow rate, slightly increases the average conversion (less than 10 %). Therefore, it is highly unlikely conversion ratios on the order of catalytic cracking reactions could ever be reached by thermal cracking[28].

The catalytic cracking of hydrocarbons is a chain reaction that can be summarized in three elementary steps: initiation, propagation and termination. The initiation step is represented by the attack of an active site on the reactant molecule to produce the

---

[5]Visbreaking is the process where the viscosity (or pour point) of crude oil or heavy fuel oil is lowered by a mild form of thermal cracking at a relatively low temperature.

activated complex, which would correspond to the formation of a carbocation in a gas phase. The chain propagation is represented by the transfer of a hydride ion from a reactant molecule to an adsorbed carbenium ion. Finally, the termination step corresponds to desorption of the adsorbed carbenium ion to give an olefin whilst restoring the initial active site[29].

The strongly acidic environment of catalytic cracking produces a very different mix of products, such as high yields of propylene and lower olefin yields. For instance, cracking catalyzed by silica-alumina gives a very low olefin yield and cracking catalyzed by zeolites can result in products that are almost free of olefins[27]. The lower olefin yields of catalytic cracking are due to rapid hydrogen transfer from:

a. Cycloparaffins and cycloolefins, which are thereby converted to aromatics;

b. Olefins, which undergo dehydrogenation and cyclization to give cycloolefins; and

c. Dehydrogenation of aromatics and olefinic species to yield coke.

These last conversions may occur through many repetitions of reaction accompanied by dimerization, condensation, and cyclization and are called secondary reactions[27].

When hydrocarbons contact strong acids, a side reaction occurs forming a high molecular weight, highly unsaturated material, called coke. Coke formation on cracking catalysts causes severe cracking activity loss. The rate of coke formation is directly proportional to the increase of acidity in a catalyst. Therefore, higher acidic catalysts, such as zeolites are expected to deactivate faster than there less acidic counter-parts, such as silicoaluminophosphate (SAPO) molecular sieves. Coke can be removed by oxidation in a fluidized-bed regenerator. In thermal cracking, coke can be formed from monoolefins by dehydrogenation and cyclization reactions proceeding through carbonium-ion intermediates. Unlike catalytic cracking, condensation and cyclization reactions occur to only a small extent in thermal cracking, as indicated by the presence of aromatic tar[27].

To maintain the overall hydrogen balance in the cracking process, the hydrogen that serves to saturate olefins must come from hydrocarbons that are converted into aromatics or coke. As a result, coke is a mixed blessing. Even though it causes rapid catalyst deactivation, it is also a source of hydrogen, which stabilizes the valuable lower-molecular weight products. Coke combustion can also be used to provide a heat source for endothermic cracking reactions[27].

Thus, propylene, butanes, and higher-molecular-weight olefins, along with the paraffins formed by termination of carbonium ions that have resulted from the cracking step, should be the[30] primary products of acid-catalyzed hydrocarbon cracking[27]. Coke formation is also usually a primary reaction in catalytic cracking of high molecular weight multi-ring aromatic hydrocarbons[27]. Despite having multi-rings, JP-10 is expected to act more as a branched paraffin rather than an naphthene. Therefore, coke is
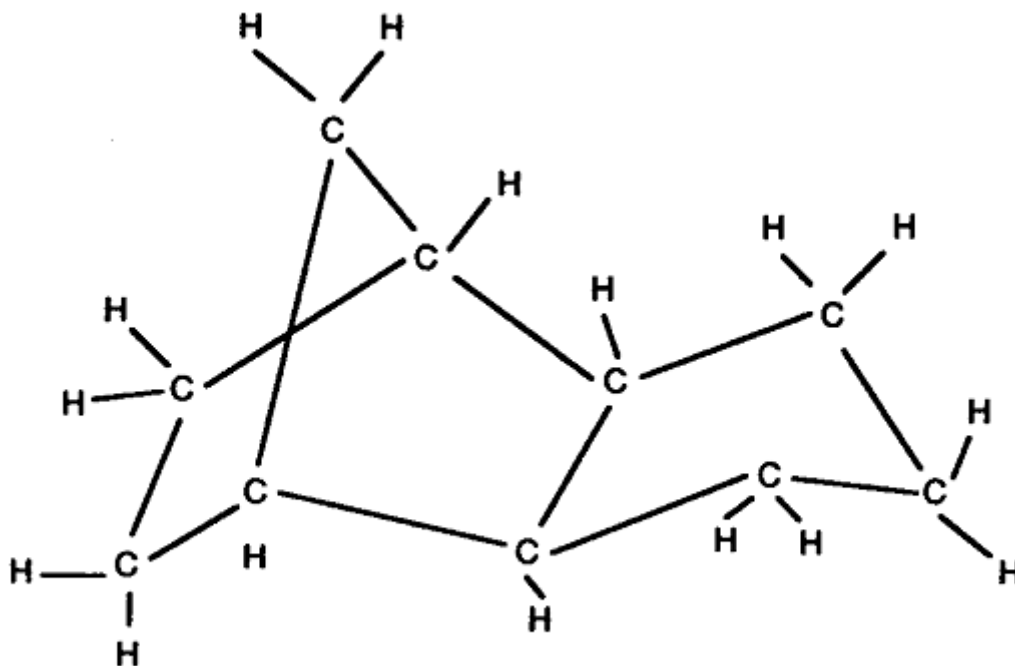
Figure 2.7 JP-10 or exo-tricyclodecane ($C_{10}H_{16}$).

not expected to be a primary cracking product. It is also known that coke formation re-
quires a source of hydrogen (coke precursor) and a sink for hydrogen (olefin)[27]. Mixed
feeds containing small amounts of polynuclear aromatics and olefins may produce more
coke than either would alone[27]. As a result, cracking a pure component hydrocarbon,
such as JP-10, should lead to less coke formation.

2.7 Decomposition Chemistry of JP-10

JP-10 or exo-tricyclodecane ($C_{10}H_{16}$), shown in Figure 2.7, is a rather unusual jet fuel as
it is composed of only one large molecule, whereas most other jet fuels contain a mixture
of hydrocarbons. Although the single molecule makes modelling the initial cracking
mechanisms easier, it is too large a 4.2molecule for a complete detailed description
of the reaction mechanisms[31]. Under pyrolysis conditions it is assumed that the
initial scission is between a C-C bond rather than an H-abstraction or C-H bond-
scission[6, 12, 31, 32].

Green et al.[33] studied high-temperature JP-10 pyrolysis using a micro flow tube
reactor and gas chromatography/mass spectrometer (GC/MS) for analysis. A heated
quartz tube was used to eliminate possibilities of surface reactions. With a 2 ms res-
idence time, JP-10 begins to decompose above 900 K, and is mostly decomposed by

1300 K[33]. Initially, the major product was cyclopentadiene (CPD); however, CPD is unstable at high temperatures and is quickly transformed into other products. At higher temperatures, the major products were benzene, propyne, and C_4H_x (x = 4, 6, 8), with smaller amounts of C_7H_x (x = 6, 8, 10) and a variety of C_8 and C_{10} species. Some minor products with higher retention times than JP-10 could not be identified with certainty on the MS spectra; however, it was concluded that these large molecules are more than likely highly unsaturated and possibly aromatic. From the pattern of products observed, it is clear that at high temperatures dehydrogenation[33] and cyclization reactions are present, in addition to the main processes leading to ring opening.

Davidson et al.[32] investigated the post-shock gas mixtures of pure JP-10 in a single pulse shock tube at conditions between 1.2 atm to 1.5 atm and 1100 K to 1700 K. High-speed UV absorption spectrum of JP-10 decomposition products showed evidence of cyclopentene as an initial decomposition product with near unity yield[32]. This result is supportive of the hypothesis that the first step of the decomposition path for JP-10 is the breaking of a C-C bond and the formation of cyclopentene[32]. Due to the short test time ($\sim$ 50 ms) the spectra did not show other products, such as benzene, because these are expected to form through secondary chemical reactions[32].

Both these studies were carried out at the high temperatures required to thermally crack JP-10, which far exceeds onboard engine capabilities. This suggests, despite the probability of a higher olefin and lower aromatic product yield with thermal cracking, catalytic cracking will be more likely to meet PDE application requirements.

Secondary reactions, such as cyclization, are a major issue in this study. Trying various catalysts with different acidity properties and varying reaction parameters can drastically change product selectivity. This study has only looked at the various catalyst activities, selectivity and effects on varying amounts of catalyst. All other experimental parameters were kept constant. This study will be using GC and GC/MS, a slower type of analysis; therefore, GC/MS spectra are expected to show the more stable products, such as benzene, other aromatics, and propylene.

2.8   Hydrocarbon Product Analysis Methods

2.8.1   Gas Chromatography Theory

The first gas chromatograph was developed commercially by James and Martin in 1952[34]. It is an instrument for separating components of mixtures of volatile compounds. A stream of inert gas, the carrier gas, passes continuously through a column. The chromatographic column is a long hollow tube that contains a thin layer of a non-volatile chemical (the stationary phase). This permeable absorbent is either coated onto the walls of the column (capillary column) or coated onto an inert solid that is

then added to the column (packed column)[34]. As the sample and carrier gas (the mobile phase) travel through the column, the sample components are retarded due to their affinity for the stationary phase. When a vapor first reaches the column it is largely adsorbed, but equilibrium is set up between the stationary and mobile phase in the interstices of the column. A portion of the sample always remains in the gas phase and moves a little further along the column in the carrier gas stream, where again it equilibrates with the column. At the same time, material already adsorbed in the column re-enters the gas phase so as to restore equilibrium with the clean carrier gas[35]. The temperature of the oven in which the GC column resides is usually increased at $4\,^{o}$/min to $20\,^{o}$/min so that higher boiling and more strongly retained compounds are successively released. A component that spends little time in the stationary phase will elute quickly. Only those materials that can be vaporized without decomposition are suitable for GC analysis[34].

The effectiveness of a chromatographic column in separating two solutes is dependent on the relative rates at which the species elutes[35]. The degree the solutes are distributed between the mobile and stationary phases determines these relative rates and is defined by distribution equilibrium. The distribution law is the ratio of the molar concentration of the solute in the stationary phase over the molar concentration in the mobile phase:

$$K = \frac{C_S}{C_M} \tag{2.1}$$

The retention time is the time it takes a molecule to traverse the entire length of the column and enter the detector. The linear rate (v) of a solute molecule is defined as the column length (L) divided by its retention time (t_R):

$$v = \frac{L}{t_R} \tag{2.2}$$

The migration rate at which a component molecule travels through the column varies with the linear velocity of the mobile phase (t_M):

$$v = \mu t_M \tag{2.3}$$

The linear rate μ of the mobile phase is determined by the carrier gas flow rate specified by the user. Only the distribution coefficient varies for each component in the same sample and is responsible for the component's varying elution times. The fraction can also be expressed as moles of solute in the mobile phase divided by the total moles of solute. Total moles of solute in the mobile phase are equivalent to the concentration of solute multiplied by the volume of the mobile phase. Likewise, the total moles of solute is the sum of moles in the mobile and stationary phase:

$$v = \frac{\mu(C_M V_M)}{(C_M V_M) + (C_S V_S)} \tag{2.4}$$

or

$$v = \frac{\mu}{1 + (C_S V_S)(C_S V_S)} \tag{2.5}$$

By substituting the distribution constant for the ratio of solute concentrations, a relation expressing a solute migration rate as a function of its distribution constant is derived:

$$v = \frac{\mu}{1 + (K + \frac{V_S}{V_M})} \tag{2.6}$$

If the sample contains only a negligible amount of non-volatile components, the component elution order will typically follows Raoult's law and elutes in the order of increasing boiling points[35].

As the component travels through the column, it diffuses over a certain volume or time interval. The signal is then recorded as a spike with a height proportional to the injected amount. The retention time is usually calculated from the highest intensity on the peak. Signal analysis can be difficult when components have similar retention times. Broad signals may result in overlapping peaks. The column resolution refers to the ability the chromatographic column separates a mixture of compounds. This can be quantified by comparing the two retention times and the variance of the eluted peaks:

$$R_S = \frac{\Delta z}{(W_A + W_B)} \tag{2.7}$$

Where Δz is the difference in time between two chromatographic peaks and W_X represents the peak widths (in time units) of the two compounds. Two frequent phenomena related to non-symmetrical (or non-gaussian) peak shapes that occur are fronting and tailing. This can most often be solved by manually decreasing the sample size or by using the split ratio mode. In the splitless mode, all of the sample is introduced onto the column. A simple means of diluting the sample is to use the split mode, where a user can specify the fraction of the sample to be introduced onto the column:

$$Split\ Ratio = \frac{Split\ Flow}{Column\ Flow} \tag{2.8}$$

By setting the split ratio and the column flowrate the split flow and the total flow are constrained. The inlet pressure is constrained by the used specified column flow and the

colmn dimensions. The average column velocity is calculated from the flow, pressure, and column dimensions. The suggested sample sizes for capillary columns should be smaller than 10^{-7} g corresponding to less than 7×10^6 μL of JP-10. This study used a 100 ul sample volume, in general, most peaks were guassian shaped (symmetrical); however, some tailing of the JP-10 was observed.

Flame Ionization Detector

After the sample is separated, the components are sent to the detector that is attached to the end of the column. The detector measures the time of elution and determines the quantity of the sample for each component.

There are two classes of detectors: those that are independent of sample concentration and those that are dependent on concentration. The latter depends on the mass flowrate of the sample rather than concentration. The detector used is based on different factors, such as sensitivity, response time, and component detectability. There are a variety of detectors available for a GC. The two most popular are the flame ionization detector (FID) and the thermal conductivity detector (TCD). The flame ionization detector (FID) was chosen for this application because it is sensitive to almost all molecules that contain hydrocarbons and has a wide range of linearity.

FID can detect compounds that contain the low ppb to high ppt. The analyte in the effluent is passed through a flame produced by igniting a hydrogen/air gas mixture[34]. Gases burning in a flame form an appreciable concentration of electrons resulting from ionization[35]. This causes a current to flow by decreasing the resistance in the gap between two electrodes. The conductivity of a hydrogen flame is exceptionally small; so when an organic vapor enters the flame the conductivity increases[35]. This amplified current flow produces a signal that can be measured and recorded. The FID is a destructive detector and is sensitive to water. Therefore, after a period of non-use, the GC oven had to be heated to 250 ^{o}C for approximately 15 min to ensure the column contained no humidity.

2.8.2 Mass Spectrometer Theory

A mass spectrometer is an instrument that measures the mass-to-charge ratio (m/z) of gas phase ions[34] to provide information about the molecular weight of the compound and its chemical species. The most common and the one in use in the Varian series MS interfaced to a GC is a quadrople. All mass spectrometers consist of three distinct regions: an ionizer, an ion analyzer, and a detector. Ions of a particular mass/charge ratio that reach the detector at a certain voltage combination. The ionizer separates gas phase ions in a low-pressure environment by the interaction of an electrical field on the charged particles[34], called Electron Impact (EI) Ionization. A high-energy electron

beam (70 eV) bombards the gas molecules exiting the GC capillary column. An electron that strikes a molecule may impart enough energy to remove another electron from that molecule. EI ionization usually produces singly charged ions containing one unpaired electron. A charged molecule that remains intact is called the molecular ion. The energy from the EI destabilizes the molecule causing further chemical bond breakage in that ion that creates molecular fragments.

The measurement is calibrated against ions of known m/z[34]. The calibrated scale is in Daltons (atomic mass units) because the EI ionization produces single charged particles so the charge (z) is almost always one.

The ion analyzer or the quadrople mass filter in this case, derives its name from the four precisely machined rods that the ions must pass between to reach the detector[34]. Ions enter the quadrople rods along the z-axis after being drawn out of the ion source by a potential (typically a few volts) [34]. The ions entering the quadrople are sorted by imposing rf/dc fields on diagonally opposed rods. By sweeping the rf/dc voltages in a fixed ratio, usually from low to high voltages, ions of successively higher masses travel the stable path shown by the solid line to the detector[34]. At any given field strength, only ions in a narrow m/z range reach the detector. All others are deflected into the rods[34]. The detector produces an electronic signal when struck by an ion. The signal is integrated with the scanning voltages to allow the instrument to report which m/z strikes the detector. The mass analyzer sorts the ions according to m/z and the detector records the abundance of each m/z.

Interpreting Mass Spectra

EI ionization introduces a large amount of energy into molecules that produces superior fragmentation. The fragments of a molecule generate information about the structure of the compound, even though the molecular ion does not often appear or is a smaller peak in the spectrum. Spectra become complicated as initial fragments undergo further fragmentation and/or rearrangements occur. On a MS spectrum, the x-axis is the increasing m/z ratio and the y-axis is the relative abundance of each ion, which is related to the number of times an ion of the m/z ratio strikes the detector. The most abundant ion is assigned a relative abundance of 100 %.

The Varian GC/MS is installed with the Varian Star Workstation analysis computer program. The Star Workstation database is contains with thousands of reference spectra, of which were used to compare and interpret the reaction products.

2.9 Catalysts

The popularity of using catalysts in the oil refining process has provided major research base for choosing the best candidate to crack JP-10. In this study, a recent form of a common zeolite and two forms of the lower acidic aluminosilica based catalyst were chosen. However, only due to time constraint were other catalyst options not explored.

2.9.1 Zeolites

Zeolites are naturally occurring microporous crystalline oxides that demonstrate spectacular catalytic properties. Many are now recreated in laboratories along with zeolites that do not naturally occurring[2, 36]. Zeolites are usually used as adsorbents and ion-exchange materials[2] and were first employed in the 1960s for catalytic cracking of petroleum[2, 36].

An active site is the location on a catalyst surface where reactions take place. There are two possible types of active sites that can occur on the surface of a catalyst, Bronsted (or Bronsted-Lowry) acid sites and/or Lewis acid sites. The former is a proton (H+ ion) donor and the latter is an electron acceptor[2]. The active sites of a catalyst are the predominant force behind the nature of catalysis with respect to selectivity of the reaction products and their rates of formation. The availability of active sites is dictated y the pore size of a catalyst. Figure 2.8[6] illustrates the effects a zeolites' nanostructure has on the three types of shape selectivity during catalysis: reactant selectivity, product selectivity and transition state selectivity[2]. The active components, dispersion of active components, surface area and pore size distribution are most important in affecting the catalyst reactivity. ZSM-5 was first synthesized in 1960s and was successfully applied to numerous refining and petrochemical processes. The crystalline structure of ZSM-5, an aluminosilicate zeolite, is depicted in Figure 2.9[7].Crystalline microporous aluminosilicates, like ZSM-5, are tetrahedral units that produce a system of uniform pores and cavities of molecular dimensions[2]. ZSM-5 can be characterized by a 3-dimensional channel system resembling an array of partially overlapping tubes. The tubes have almost circular 10-ring apertures, which are depicted in Figure 2.10. Zeolites demonstrate spectacular catalytic properties, their stability and regularly sized and shaped micropores allow for their use as shape selective catalysts, which dominate many of the established and new catalytic processes[2, 37].

However, the constraint with microporous zeolites is their small pore diameter $(< 10 \ \dot{A})$[38] that does not allow the diffusion of bulkier molecules[39]. The chan-

---

[6]Concept provided by:
$http://mch3w.ch.man.ac.uk/theory/staff/student/mbdtscw/transfer_html/node6.html.$
[7]All catalyst framework diagrams were provided by iza-online.com under the GNU free documentation agreement.
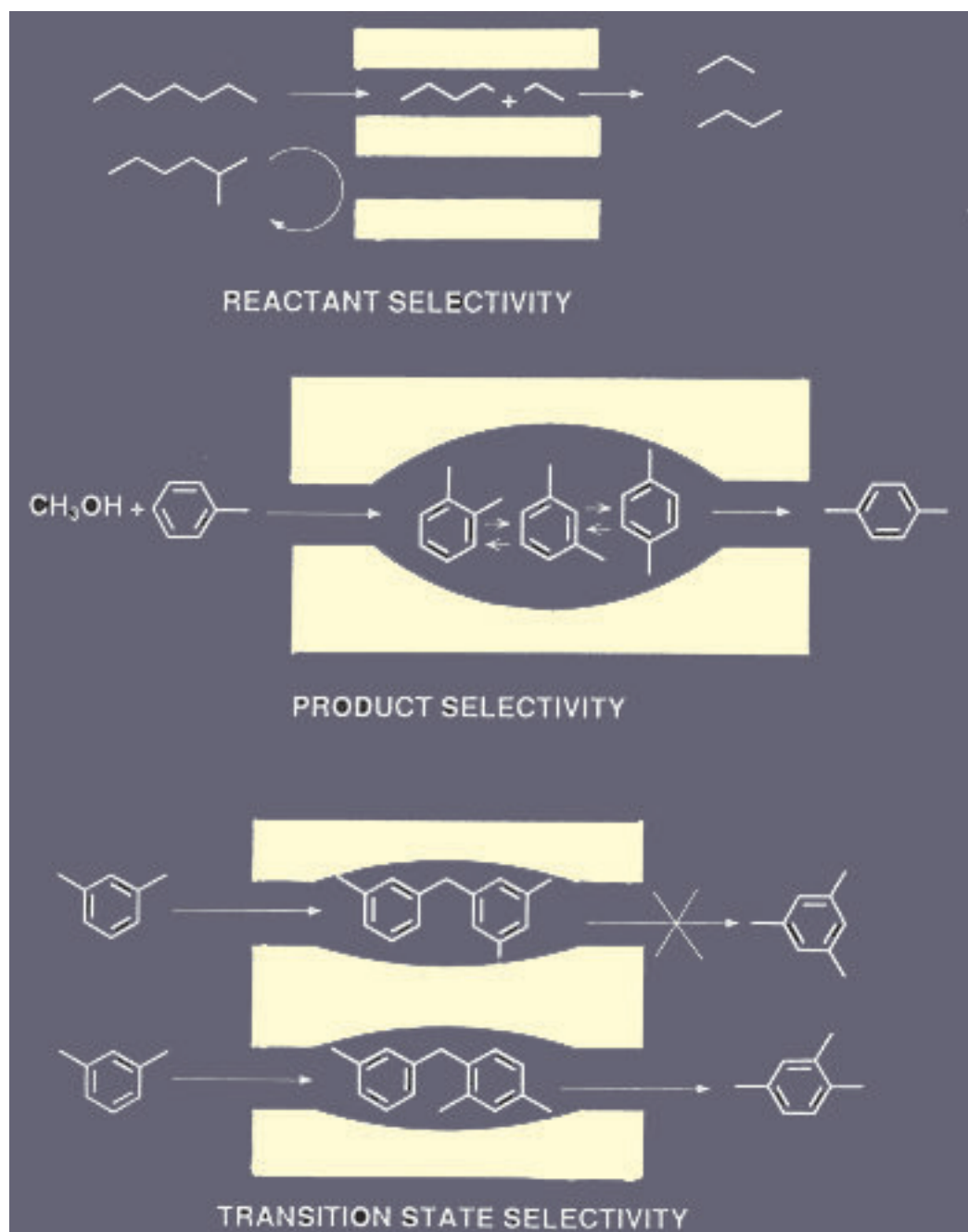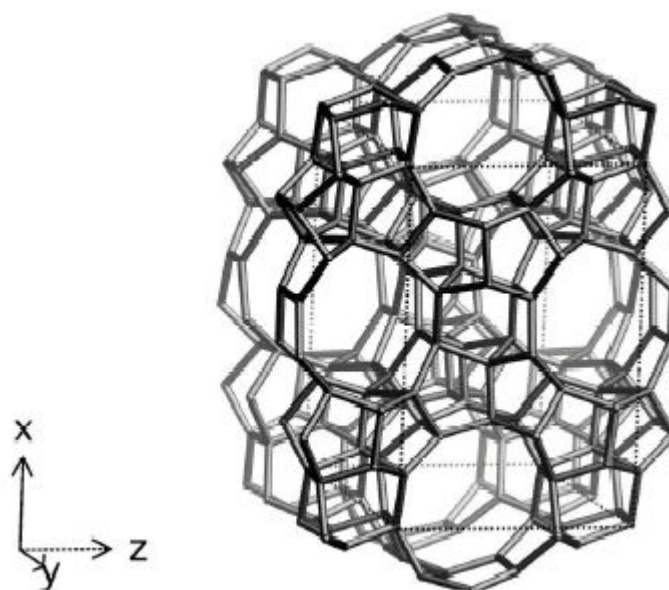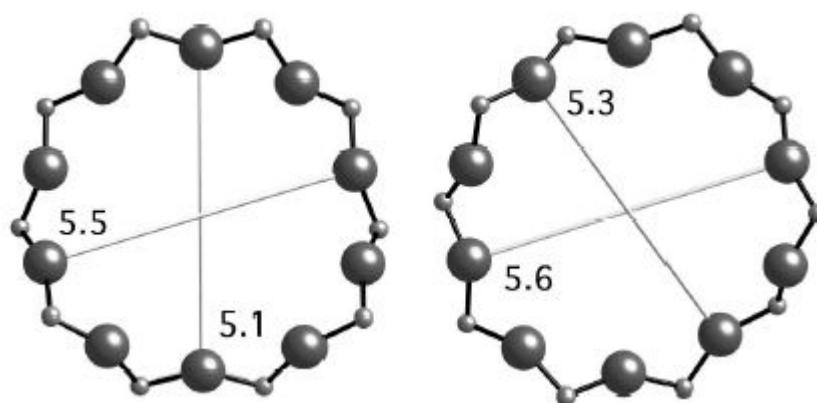
Figure 2.8 Shape selectivity effects.

Figure 2.9 ZSM-5 framework viewed along [010].

Figure 2.10 From left to right, ZSM-5 10-ring apertures viewed along [100] and [010].

nels are so small, most of the functionality is transmitted to the outer surface where there is no shape-selectivity[2]. Cooper and Shepherd[28] conducted a catalytic cracking study of JP-10 using three large-pore zeolite catalysts that are commonly used in the oil industry: HY, USY, and Beta zeolites. The highest conversion rate of 70 % was achieved with 1 g of Beta zeolite at 500 ^{o}C, using a flow rate of 2.3 g of JP-10/hr, which produced mainly $\geq C_5$ hydrocarbon products.

Although the Cooper study achieved a notable conversion rate with Beta zeolite, the commercial catalyst did not demonstrate the three most important characteristics needed for PDE applications, which are:

a. to decrease the amount of aromatics as to reduce the amount of coking;

b. to lower the C_5^+:C_4^- ratio to try to improve the detonability of the product mixture; and finally,

c. to perform JP-10 cracking in less severe conditions (especially at lower temperatures) than thermal cracking.

Nanocrystalline ZSM-5

A different approach as to the use of small pore zeolites has been to try to benefit from the external active sites. By synthesizing zeolites with crystal sizes between 10 nm and 100 nm, the external surface area and therefore, the external sites density is actually increased. The catalytic reaction would not depend on the impenetrable internal sites, but would take advantage of the easily accessed external sites. The reaction would initially take place on the external acid sites and subsequent secondary reactions may occur over both internal and external active sites[39].

A recent study conducted for the recycling of plastics showed that nanocrsystalline ZSM-5 demonstrated remarkable activity in the catalytic cracking of Low and High density Polethylene (LDPE and HDPE) and Polypropylene (PP) at low temperatures ranging from 340 ^{o}C to 380 ^{o}C[39]. Gaseous hydrocarbons were the main products with a maximum centered at C_4. The selectivity towards C_3 to C_5 hydrocarbons is enhanced on decreasing the cracking temperature, reaching a 95 % to 100 % at 340 ^{o}C. Analyses of liquid hydrocarbons obtained at higher temperatures (380 ^{o}C) indicate that the highest amount of olefins (47 %) is obtained in the cracking of the linear HDPE. In contrast, the branched PP leads to more aromatic compounds (38 %)[39].

Having unusual molecular structure, JP-10 is expected to react more like a branched paraffin rather than an olefin napthene (cycloparaffin). Therefore, a rather high amount of aromatics, as seen with branched PP, is expected. However, the importance of this study is drawn from the result that the selectivity for C_3 to C_5 is seen at the lower temperatures. Lowering the temperature lowers secondary reaction acitivity, which as mentioned earlier produces coke and aromatics. The ability to crack JP-10 into a

higher olefin to aromatic ratio mixture at low temperature would mean only a low-energy onboard heat source would be required for a catalytic reactor in a PDE.

2.9.2 Silicoaluminophosphate Molecular Sieves

Silicoaluminophosphate (SAPO) molecular sieves are a class of acidic crystalline microporous materials generated by the introduction of silicon into an aluminophosphate framework[40]. The silicon species, which partially substitute the phosphorous in the neutral aluminophosphate framework structure, produce negative charges. Bronsted acid sites are generated by decomposing the organic cations during calcination. The organic cations are used as a template during synthesis and remain in the structure compensating for some of the framework charges. Substituting the cations generates a certain number of protonic sites[41].

Fernandes et al.[40] conducted a study of the catalytic ability of SAPO-37 molecular sieve to degrade polyethylene. A high conversion rate was achieved with 26.4 % of the product yield being C_3 and C_4 hydrocarbons. The success of this study led to the focus on SAPOs to attempt to reduce the yield of larger hydrocarbons and aromatics in the catalytic cracking of JP-10.

SAPO-5 and SAPO-11 were synthesized in the present study. Their pore system frameworks are depicted in Figures 2.11 and 2.12, respectively. Like ZSM-5. SAPO-5 has a circular aperture, but with a 1-dimensional 12-ring channel system, as shown in Figure 2.13. The slightly larger pores with a less complicated pore structure should allow the diffusion of the JP-10 molecule. SAPO-11 is characterized by a 1-dimensional channel system with elliptical 10-ring apertures, as shown in Figure 2.14.

It was also desired to produce SAPOs with smaller pores in order to take advantage of the external acid sites, as with nZSM-5. The two SAPOs were chosen because they are less acidic than nZSM-5, which should reduce the occurence of secondary reactions. Crystallization time and temperature have a significant impact during SAPO synthesis. Therefore, in attempt to reduce the pore size of SAPO-11 and SAPO-5 several synthesis varying these two parameters were performed. The crystallization parameters reported in this work yielded the most crystallized catalysts with few impurities.

2.10 Catalyst Characterization

Four analysis techniques were used to characterize the synthesized catalysts: X-ray diffraction (XRD); Brunauer-Emmett-Teller (BET) analysis of nitrogen adsorption isotherms; scanning electron microscope (SEM); and pyridine chemisorption. Not only is XRD spectra used as simple method for catalyst identification, but can also be used to correlate crystal size with the peak width and used to compare the crystallinity between the
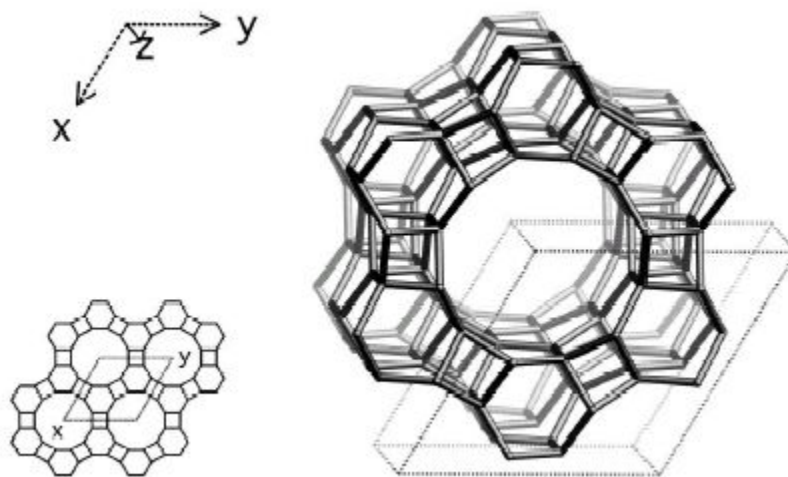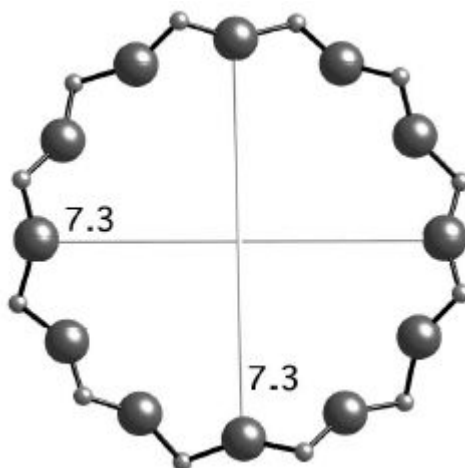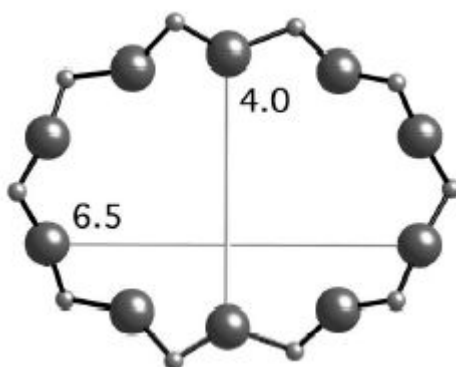
Figure 2.11 SAPO-5 framework viewed along [001].

Figure 2.12 SAPO-11 framework viewed along [100].

Figure 2.13 SAPO-5 12-ring aperture viewed along [001].

Figure 2.14 SAPO-11 10-ring aperture viewed along [001].

synthesized catalysts with the same structure. BET adsorption analysis is used to to characterize the specific surface area, total pore volume, and pore size distribution of the catalysts. SEM is used to quantify the crystal size, clarify the crystal structure and give a qualitative analysis of the catalyst purity. FTIR analysis of adsorbed pyridine is used to characterize the acidic properties of a solid catalyst.

2.10.1   X-ray Diffraction

The most frequently used method for identifying and describing structures of zeolitic type material is the X-ray powder diffraction (XRD). The simplicity of the powder diffraction technique is easily applied to the small crystal structure of zeolites where single crystal methods cannot be used[42].

X-rays are electromagnetic radiation of wavelength $\sim 1 \dot{A}$ that occur between gamma-rays and the ultra-violet on the electromagnetic spectrum. This wavelength is approximately the same length as the diameter of an atom, making it ideally suited for probing the structural arrangement of atoms and molecules in a wide range of materials. The energetic X-rays penetrate deep into the materials and provide information about the bulk structure.

X-rays are produced generally by either X-ray tubes or synchrotron radiation. In a X-ray tube, which is the primary X-ray source used in laboratory instruments, X-rays are generated when a focused electron beam, accelerated across a high voltage field bombards a stationary or rotating solid target. As electrons collide with atoms in the target and slow down, a continuous spectrum of X-rays are emitted, which are termed Bremsstrahlung radiation. The high energy electrons also eject inner shell electrons from the atoms through the ionization process. When a free electron fills the shell, an X-ray photon, with energy characteristics equal to the target material, is emitted. Common targets used in X-ray tubes include Cu and Mo, which emit wavelengths of 1.54 $\dot{A}$ and 0.8 $\dot{A}$, respectively. The energy E of an X-ray photon and it's wavelength (λ) are related by Equation 2.9:

$$E = \frac{hc}{\lambda} \tag{2.9}$$

where h is Planck's constant, and c is the speed of light.

If the wavelength of the emitted X-rays did not change upon collision with an atom (X-ray photons did not lose any energy, only momentum was transferred), the process is called elastic scattering or Thompson Scattering. These are the X-rays that are measured in diffraction experiments. On the other hand, in the inelastic scattering process or Compton Scattering, X-rays transfer some of their energy to the electrons and the emitted X-rays have a different wavelength than the incident X-rays. The emitted X-rays carry information about the electron distribution of the target material.
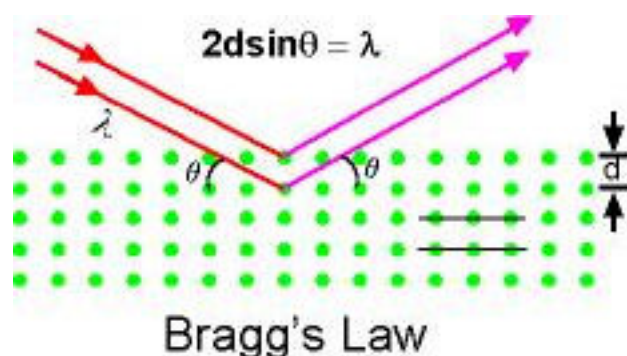
Figure 2.15 Geometric derivation of Bragg's Law

Diffracted waves from different atoms can interfere with each other. The resultant intensity distribution is strongly affected by this interaction. If the atoms are arranged in a periodic fashion, as in crystals, the diffracted waves will consist of sharp interference peaks with the same symmetry as in the distribution of atoms. Thus, the distribution of atoms in a material can be deduced by measuring the diffraction pattern.

Powder X-ray Diffraction (XRD) is perhaps the most widely used XRD technique for characterizing materials. As the name suggests, the sample is usually in a powdery form, consisting of fine grains of single crystalline material. The technique is also used widely for studying particles in liquid suspensions or polycrystalline solids (bulk or thin film materials).

The term 'powder' simply means that the crytalline domains are randomly oriented in the sample. When the 2-D diffraction pattern is recorded, it displays concentric rings of scattering peaks corresponding to the various spacings (d) in the crystal lattice. The positions and the intensities of the peaks are used for identifying the underlying structure (or phase) of the material. For example, the diffraction lines of graphite would be different from diamond even though they both are made of carbon atoms. This phase identification is important because the material properties are highly dependent on structure.

The peaks in a X-ray diffraction pattern are directly related to atomic distances. Therefore, the size and shape of the unit cell for any compound can easily be determined using the path difference between two waves. Equation 2.10 gives the path difference between two wavelengths. It is geometrically derived using the laws of diffraction as shown in Figure 2.15:

$$\lambda = 2d sin\theta \qquad (2.10)$$

However, for constructive interference between these waves, the path difference must be an integral number of wavelengths, which leads to:

$$2dsin\theta = n\lambda \tag{2.11}$$

Equation 2.11 is known as the Bragg's law, where λ is the wavelength of the X-ray, θ the scattering angle, and n an integer representing the order of the diffraction peak. Bragg's Law is one of the most important laws used for interpreting X-ray diffraction data.

Bragg's Law applies to scattering centers consisting of any periodic distribution of electron density. In other words, the law holds true if the atoms are replaced by molecules or collections of molecules, such as colloids, polymers, proteins and virus particles.

From the XRD spectra an important correlation of the peak broadening with the crystal size can be calculated using the Scherrer equation:

$$D = \frac{k\lambda}{\beta cos\Theta} \tag{2.12}$$

where D is the particle size in angstroms, k is a constant approximately equal to unity if β is the half-maximum peak breadth in radians, λ is the wavelength of the x-rays in angstroms, and Θ is the Bragg angle of the same peak used to calculate β[43].

2.10.2 Nitrogen Adsorption

Specific surface area and the porosity of catalysts can be determined by applying the nitrogen adsorption and desorption method at the temperature of liquid nitrogen. The surface area of a powder or solid can be calculated using the Brunauer-Emmett-Teller (BET) Equation 2.13:

$$\frac{1}{W(\frac{P_o}{P} - 1)} = \frac{1}{W_m C} + \frac{C - 1}{W_m C}(\frac{P}{P_o}) \tag{2.13}$$

Where W is the weight of gas absorbed at the equilibrium pressure P; P_o is the vapour pressure at saturation of the adsorbate at the adsorption temperature; and W_m is the weight of adsorbate consituting a monolayer of surface coverage. The BET constant C is related to the heat of adsorption corresponding to the first layer of adsorbate and to the heat of condensation of the adsorbate. Therefore, its value is an indication of the magnitude of the adsorbent/adsorbate interactions[44].

A multi-point linear plot was developed by using:

$$\frac{1}{[W(\frac{P_o}{P} - 1)]} \ vs \ \frac{P}{P_o} \tag{2.14}$$

For most solids this plot is restricted to a limited region of the adsorption isotherm where the slope is linear: in this study the P/P_o range was limited to between 0.05 to 0.30[44]. The value of W_m is obtained from the slope $P/W(P^o-P) = f(P/P^o)$, which is equal to C - $1/W_m$, and from the coordinates of the origin $1/W_m C$.

The weight of a monolayer of adsorbate (W_m) is obtained from the slope (m) and the intercept (I) of the BET plot:

$$m = \frac{C-1}{W_m C} \tag{2.15}$$

$$I = \frac{1}{W_m C} \tag{2.16}$$

Thus, the weight of the monolayer (W_m) is obtained by combining equations 2.15 and 2.16:

$$W_m = \frac{1}{m+I} \tag{2.17}$$

Finally, the surface area is calculated by using the molecular cross-sectional area (A_{cs}) of the adsorbate molecule. The total surface area (S_t) of a solid sample is expressed as:

$$S_t = \frac{W_m N A_{cs}}{M} \tag{2.18}$$

where N is Avogadro's number (6.023×10^{23} molecules/mole) and M is the molecular weight of the adsorbate. The most common gas adsorbate used for BET surface area determination is nitrogen. For the hexagonal close-packed nitrogen monolayer at 77 K, the cross-sectional area (A_{cs}) for nitrogen is 16.2 A^2[44].

The specific surface area (S) of the solid is calculated from the total surface area (S_t) and the sample weight (w) according to Equation 2.19:

$$S = \frac{S_t}{w} \tag{2.19}$$

Porosity of powders and other porous solids can be also be characterized by gas adsorption. Porosity is often described by total pore volume and pore size. Pore size can be categorized in three sizes: macropores, mesopores and micropores. Macropores are pores with openings larger than 500 $\dot{A}$, micropores are pores with openings no larger than 20 $\dot{A}$ and pores between 20 $\dot{A}$ and 500 $\dot{A}$ are mesopores[44].

The quantity of adsorbate on a surface is measured over a wide range of relative pressures at a constant temperature to obtain an adsorbtion isotherm. The adsorbent is exposed to a known quantity of nitrogen at 77 K and the quantity of gas removed from the sample is measured as the relative pressure is lowered[44].

Total pore volume is derived from the amount of vapor adsorbed at a relative pressure close to unity, by assuming that the pores are filled with liquid adsorbate. If the solid contains no macropores the isotherm will remain nearly horizontal over a range of P/P_o approaching unity and the pore volume is well defined. However, in the presence of macropores the isotherm rises rapidly near $P/P_o = 1$ and in the limit of large macropores may exhibit a vertical rise. In this case the limiting adsorption can be identified reliably with the total pore volume assuming careful temperature control of the sample[44]. The volume of nitrogen adsorbed (V_{liq}) contained in the pores using Equation 2.20:

$$V_{liq} = \frac{P_a V_{ads} V_m}{RT} \qquad (2.20)$$

in which P_a and T are ambient pressure and temperature, respectively, and V_m is the molar volume of the liquid adsorbate (34.7 cm^3/mol for nitrogen). Since pores that would not be filled below $P/P_o = 1$ have a negligible contribution to the total pore volume and the surface area of the sample, the average pore size can be estimated from the pore volume[44]. For example, assuming cylindrical pore geometry, the average pore radius (r_p) can be expressed by Equation 2.21:

$$r_p = \frac{2V_{liq}}{S} \qquad (2.21)$$

where V_{liq} is obtained from Equation 2.20 and S is the BET surface area (Equation 2.19)[44].

2.10.3   FTIR Analysis of Chemisorbed Pyridine

Fourier Transform Infrared (FTIR) spectroscopy is extensively used to characterize the acidic properties of catalysis by adsorption. A frequently used adsorbate is pyridine. Bronsted and Lewis acid sites can easily be distinguished by the different IR peaks produced from chemisorption. For instance, pyridine produces a band around 1540 cm^{-1} when adsorbed on Bronsted acid sites, resulting in the formation of pyridinium ion. Pyridine attached to Lewis acidic centers such as $Al_x O_y{}^{n+}$ gives rise to a typical band at about 1450 cm^{-1}. Adsorption of pyridine on cations of zeolite structures produces bands in the range from 1438 cm^{-1} to 1452 cm^{-1}. The exact positions of these bands depend on the nature of the cation, that is, on the Coulomb potential (q/r), where

q is the electric charge and r is the radius of the respective cation). Adsorption and desorption of water (hydration and dehydration) may also be easily monitored by IR, since adsorbed H_2O gives rise to a typical deformation band around 1640 cm^{-1}[45].

2.10.4   Scanning Electron Microscope

The scanning electron microscope (SEM) provides valuable information about the microstructure characteristics of solids including the purity and homogeneity of the final product. Small amounts of amorphous material that is not detectable by XRD are more easily distinguished. SEM investigation leads to important information of crystal shape, size and distribution, the nature of inter-growth and over-growth crystalline impurities[42].

The Scanning Electron Microscope creates magnified images by using electrons instead of light waves as used by traditional microscopes. The SEM shows very detailed 3-dimensional black and white images at much higher magnifications than is possible with a light microscope. If the samples are not made out of a conductive material, the samples are coated with a very thin layer of gold by a machine called a sputter coater. The sample is placed inside the microscope's vacuum column through an airtight door. After the air is pumped out of the column, an electron gun emits a beam of high-energy electrons from the top. This beam travels downward through a series of magnetic lenses designed to focus the electrons to a very fine spot. Near the bottom, a set of scanning coils moves the focused beam back and forth across the specimen, row by row. As the electron beam hits each spot on the sample, sec[30]ondary electrons are knocked loose from its surface. A detector counts these electrons and sends the signals to an amplifier. The final image is built up from the number of electrons emitted from each spot on the sample.

Chapter 3

Experimental

3.1 Synthesis

The synthesis for nZSM-5 was the least complicated as the procedure was provided by Grieken et al.[36], which when followed concisely yields the desired product. SAPO syntheses were based on verified procedures by commissions from the International Zeolite Association (IZA). Low Si/Al ratios (0.3 and 0.17 for SAPO-5 and SAPO-11, respectively), lower crystallization temperatures, and longer crystallization times were used in an attempt to reduce pore size and, to develop a well ordered and highly porous structure. Tables 3.1 and 3.2 show the batch composition and crystallization parameters of the five successfully synthesized catalysts used in this study.

Table 3.1 Gel Composition.

Catalyst	P	Si	Al	H_2O	Template
nZSM-5	-	60 TEOS*	Al_2SO_4	15	21.4 TPAOH**
SAPO-5	5.9 H_3PO_4	SiO_2	0.3 Boehmite	2.3	0.8 Pr_3N***
SAPO-11	H_3PO_4	0.2 SiO_2	1.2 Boehmite	19.4	0.4 Pr_3N

*Tetraethylorthosilicate **Tetrapropylammonium hydroxide ***Tripropylamine

Table 3.2 Synthesis parameters of successfully prepared catalysts.

Structure		nZSM-5	SAPO-5	SAPO-11
Experimental Crystallization	Temperature ($^o C$)	170	175	177
	Time (h)	6-48	10	24
Reference Crystallization	Temperature ($^o C$)	170	200	145
	Time (h)	6-72	3	18

3.1.1 Gel Preparation

For nZSM-5, tetrapropylammonium hydroxide (TPAOH) 20 wt % solution in water was used as the structure directing agent, and tetraethylorthosilicate (TEOS) (Aldrich) and aluminum sulphate (Aldrich) were used as the silica and alumina sources, respectively[39].

The reagents used in the SAPO syntheses included: Pseudoboehmite (Catapal-B), 85 % orthophosphoric acid (Aldrich), and fumed silica. Tripropylamine was used as the structure directing agent.

A glass beaker in a fumehood at ambient temperature under constant mechanical stirring was used to prepare the gels. Details of the synthesis steps follow:

Nanocrystalline ZSM-5 Synthesis Method

The silica gel was first prepared by slowly adding 122 g 20 % TPAOH ($\sim$ 5 g/min) to 70 g TEOS. The solution must be under continuous vigorous stirring and the reactant agents must be gradually added in stages or the mixture will become very viscous and will eventually solidify. The matrix solution was left stirring uncovered at room temperature for 1.5 h in a fumehood.

8.8 g of $Al_2(SO_4)_3$ was dissolved in 30 g distilled water. The aluminum solution was then added gradually ($\sim$ 1 g/min) to the silica gel under vigorous magnetic stirring. The final solution was left stirring overnight uncovered at room temperature in a fumehood to ensure an evenly distributed solution.

SAPO-5 Synthesis Method

The SAPO-5 gel was prepared following the procedure outlined by Young and Davis[46]: 11.53 g of H_3PO_4 was diluted with 41.9 g H_2O; and, 7.3 g catapal B was added ($\sim$ 0.25 g/min) to the H_3PO_4 solution under vigorous magnetic stirring. The catapal solution was left to stir for overnight at room temperature covered with a glass dish in a fumehood.

A solution of 1.2 g SiO_2 dissolved in 14.6 g Pr_3N was added to the catapal slurry ($\sim$ 0.5 g/min). Finally, the final matrix solution was stirred for 3 h uncovered at room temperature in a fumehood.

SAPO-11 synthesis Method

The SAPO-11 gel was prepared following the procedure outlined by Szostak et al.[47]: 10.4 g H_3PO_4 was diluted with 27 g H_2O; and, 7.2 g Catapal B was then added to the

H_3PO_4 solution ($\sim$ 0.25 g/min) while being vigorously stirred with a magnetic stirrer. The catapal solution was left to stir for 30 min at room temperature, lightly covered in a fumehood.

A solution of 1.2 g fumed SiO_2 was well mixed in 18 g H_2O. This silica solution was then added to the catapal slurry ($\sim$ 2 g/min) and stirred for 2 h covered with a glass dish at room temperature in a fumehood.

Finally, 7.5 g n-Pr_2NH was added to the silica-aluminium solution ($\sim$ 0.1 g/min) and stirred for 2 h uncovered at room temperature in a fumehood.
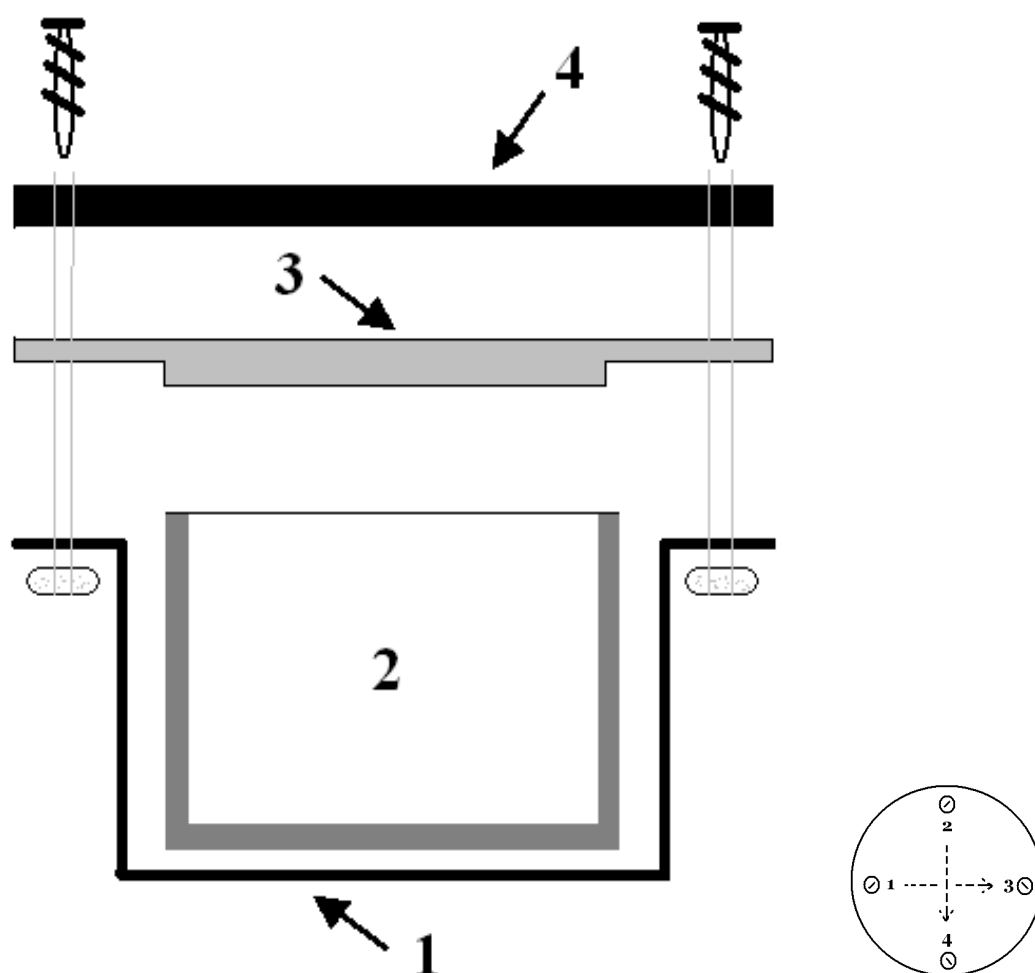
3.1.2 Crystallization

Crystallization of the catalysts were performed in a teflon lined stainless steel cylindrical autoclave shown in Figure 3.1[42].

The Teflon beaker and cover were washed by immersing them in hydrofluoric acid (HF = 49 wt %) for at least 24 h then scrubbed with a hard plastic brush and rinsed several times with distilled water. This thorough washing process ensured that there was no crystalline residue remaining on the surface of the Teflon beaker from previous syntheses.

The prepared gel was carefully poured into the autoclave, which was completely sealed by tightening the screws in a 1324 sequence (see Figure 3.1). In the case of nZSM-5, the gel was divided into two separate autoclaves. The autoclave was then put in a convection oven to be heated under its autogenous vapor pressure at the desired temperature ($\pm$ 3 ^{o}). A stopwatch was used to time the predetermined crystallization period.

3.1.3 Product Recovery

At the end of crystallization, the autoclave was removed from the oven and immersed in cold tap water for at least 15 min. Once cooled, the autoclave was opened and the distinctive yellow top layer was decanted and discarded. The rest of the contents in the Teflon beaker were poured into a one liter glass flask, mixed with distilled water, and left standing for $\approx$ 15 min. The top layer was decanted and product was separated by centrifugation. The solids that settled at the bottom quickly were simply recovered by decantation. Both recovery methods were repeated several times to ensure the product was thoroughly washed. Finally, the product was dried in a glass dish in an oven at 70 ^{o}C over night.

Figure 3.1 The stainless steel autoclave used for crystallization is comprised of four parts: 1) a cylindrical stainless steel vessel with a flange-like rim and four screw holes; 2) a 250 ml rimless teflon cylindrical beaker with 3 mm thick walls; 3) a flat Teflon cover to seal the Teflon beaker; and, 4) a stainless steel flat cover that is tightened by four screws. The autoclave was sealed by tightening the screws in a 1324 sequence[42].

3.2 Catalyst Characterization

3.2.1 X-ray Diffraction

The crystalline structure of all catalysts were determined by X-ray Diffraction (XRD). The spectra were recorded using a Phillips X-ray diffractometer consisting of a PW 1010 generator and a PW 1050 goniometer mounted on a monochromator of LiF or graphite. The copper radiation K_α with a wavelength 1.506 $\mathring{A}$ was used as the incident source. The identification of the crystalline structure of the catalysts was done by comparing the angles of diffraction of the experimental spectra with the standard values prepared by Treacy et al.[48] on behalf of the Structure Commision of the IZA.

3.2.2 Nitrogen Adsorption

An Omicron Technology Corporation Omnisorp 100 was used to determine the specific surface area and the pore volume of the catalysts. Approximately 75 mg of catalyst was first dehydrated under vacuum (0.00 Pa, 573 K, 3 h). The evacuated tube was placed in a liquid nitrogen bath and the BET program was started at atmospheric pressure using nitrogen as the adsorbate with a flow of 0.30 ml/min. The sampling rate was set for every 0.75 min until a maximum of 690 kPa (100 psi) was reached, where the desorption process began using the same settings as for adsorption.

3.2.3 Pyridine Chemisorption

Using a Bio Rad Digilab FTS-60, FTIR spectra of adsorbed pyridine were established to characterize the acidity of the catalysts. Calcined samples were first dehydrated in vacuum (0.00 Pa, 673 K, 24 h). Spectra, designated as 'before pyridine', were recorded The samples were then exposed for 10 min to pyridine vapor (60 KPa, 297 K). The excess pyridine vapor was evacuated (0.00 Pa, 473 K, 12 h). The FTIR (after pyridine) were recorded at room temperature in the evacuated cell (BioRad FTS-60) with a 4 cm^{-1} resolution[49].

3.2.4 Scanning Electron Microscope

A Jeol JSM 840A scanning electron microscope equipped with an EDAX analyzer was used to obtain crystal micrographs of all five catalysts. The powder sample was directly pasted on a metallic support with epoxy adhesive and coated with a very thin film of gold using a high-vacuum chemical vapor depositor. By bombarding the solids with electrons, high concentrations of electrical charges accumulate on the surface. This

surface charging gives a very glowing image of the zeolite particles. By using a thin film of gold, the image clarity improves by conducting the electrical charge accumulated on the zeolite surfaces.

3.3 Catalytic Reaction Experimental

A Benchtop Tubular Reactor System (BTRS) manufactured by Autoclave Inc. was used to carry out the catalyst tests. Catalysts were calcined in a porcelain crucible in a muffle furnace at 550 ^{o}C for 5 hours in air before being packed into the stainless steel tubular reactor as a 20/40-mesh between two quartz wool plugs. Analysis was done using a Gas Chromatograph/Mass Spectrometer (GC/MS) with a molecular sieve packed capillary colum and a GC using an OV-3 stainless steel packed column in conjunction with a flame ionization detector (FID).

A schematic of the BTRS is shown in Figure 3.2. An automated syringe was used to inject 0.001 μL/min (65 mg/min) of JP-10 into the static mixture in the reactor oven heated to 250 ^{o}C. JP-10 vapour was carried to the reaction zone by 26 ml/min of He gas. Reactions were carried out at temperatures between 250 ^{o}C and 600 ^{o}C. The minimum back-pressure that could be achieved in the reactor was 7 psi (48.25 kPa). The back-pressure increased by 1 psi (6.9 kPa) every 50 ^{o}C.

The total molar flow rate (n_T, mol/h) of the feed was calculated by adding the molar flow rate of JP-10 with the moles per hour of Helium, shown in Equation 3.1:

$$n_T = n_{He} + n_{JP-10} \tag{3.1}$$

Space velocity (WHSV) was calculated using the initial feed conditions in Equation 3.2:

$$WHSV = \frac{Q_T}{V_c} \tag{3.2}$$

where Q_T is the volumetric feed rate (Equation 3.3) and V_c is the volume of the catalyst (Equation 3.4):

$$Q_T = \frac{n_T RT}{P} \tag{3.3}$$

where R is the gas constant, T is the oven temperature (473 K) and P is the initial reaction pressure (48.25 kPa).
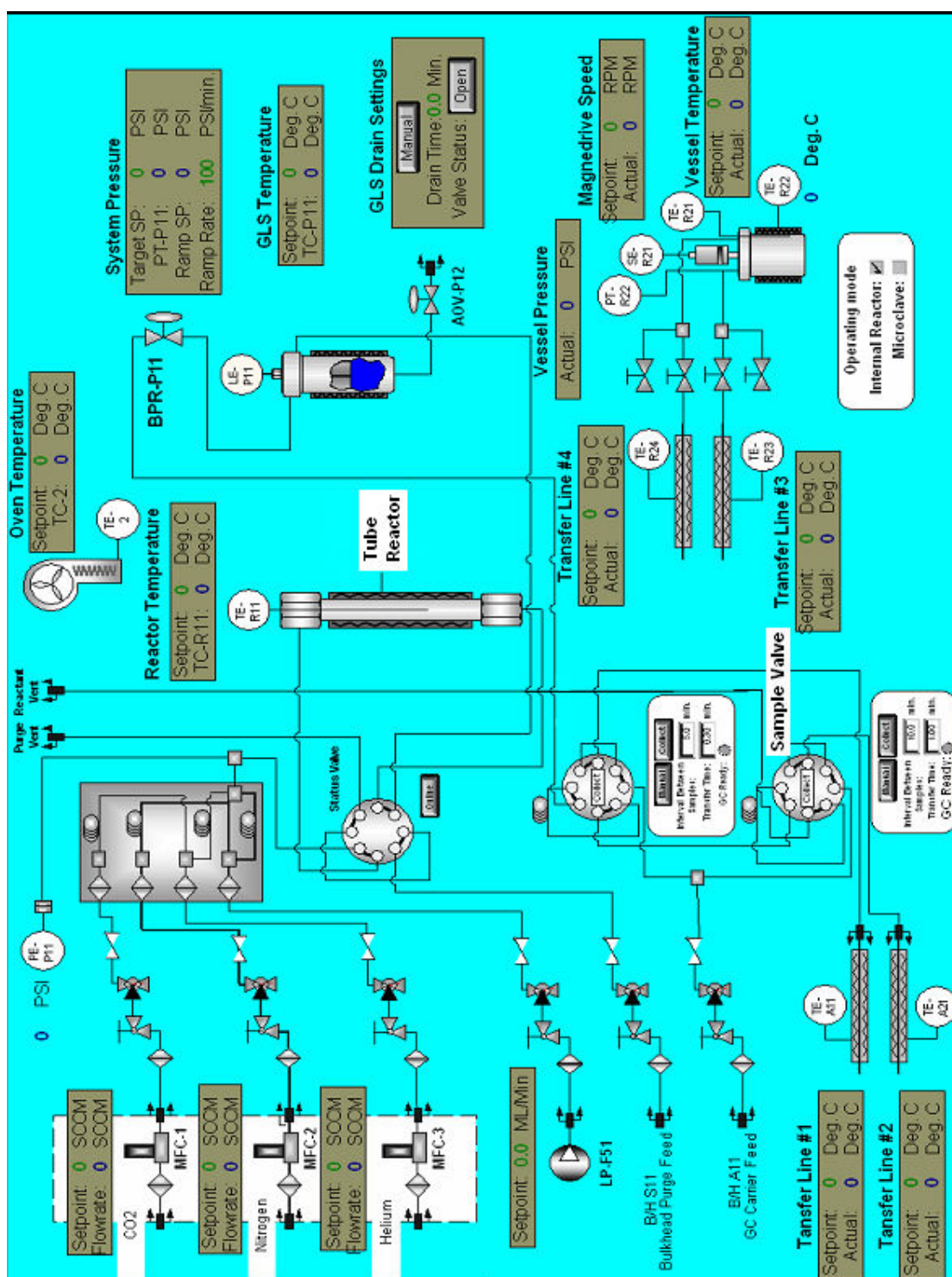
$$V_c = \pi r^2 L \tag{3.4}$$

Figure 3.2 Diagram of the Benchtop Tubular Reactor System (BTRS).

where r is the radius of the reactor tube and L is the length of the catalyst in the tube.

3.3.1 GC Operation

The Varian Star Workstation software program is used to configure the GC. System operating parameters are specified, runs are begun, and the data is required. The settings are stored in the method, which is comprised of all the data acquisition and analysis parameters specific to a given sample. A sample list was used for continuous sampling with the same set parameters of the products from the reactor.

The reactor is attached to the GC by a steel tube attached to an electronic valve system. A 0.25 ml sampling loop was installed on the line to the GC. The sample loop volume controls the amount of sample introduced on the column. This reduces the sample size to help eliminate problems of column saturation. The gas sampling valve is an easy way to produce repeatable injections of gaseous samples.

As suggested for capillary columns the flow was set to 2.0 ml/min. The flowrate affects the sample elution time from the column inlet to the detector. It is possible to optimize sample separation and lessen peak excessive peak broadening by adjusting this parameter. The inlet temperature should also be set approximately 20 ^{o}C greater than the highest boiling point temperature of the sample components. Ramping the column temperature promotes component separation and orders the elution times by their boiling point temperatures.

3.3.2 GC/MS Interface

The effluent must be transported from the GC to the MS in such a way that the analyte neither condenses in the interface nor decomposes before entering the mass spectrometer ion source. In addition the gas load entering the ion source must be within the pumping capacity of the mass spectrometer[34].

The Varian GC/MS is installed with a capillary column, where the column exit is directly inserted into the ion source. This is possible because under normal operating conditions the mass spectrometer pumping system can handle the entire effluent from the column[34]. It is necessary to heat the capillary column between the GC and the MS ion source, taking care to eliminate cold spots where analyte could condense[34]. To ensure the interface was heated above the boiling point of the highest-boiling component of the sample, the column was heated to 280 ^{o}C.

3.4 Product Identification

Most reaction products were identified by using the GC/MS Varian Inc. Star Workstation database; however, the column used in the GC/MS could not separate the light hydrocarbons ($\leq$ C$_2$). Therefore, two other methods were used to identify the reaction products. Standardized gas mixtures and solutions of liquid hydrocarbons were injected in the GC. As seen from the clearly separated peaks in Figure 3.3 the light hydrocarbons could be easily identified. Well separated peaks were also seen with the heavy hydrocarbons. An example of hexane, toluene, and p-xylene peaks on a GC trace is seen in Figure 3.4. The other method used to identify reaction products was to compare boiling points. As mentioned earlier, hydrocarbons generally elute in their order of boiling points during GC FID analysis[28].

Napthalene and xylene have been clearly identified as two of the major products of the catalytic reactions. These would both be formed from cyclization, suggesting that hydrogen would be a major product. Unfortunately, the amount of hydrogen cannot be calculated because of the columns used in the GC and GC/MS for these analysis. Hydrogen would play an important role of making a more detonable mixture and it would therefore, be most beneficial to repeat these reaction tests with hydrogen quantification in order to calculate the amount produced.

3.5 Calculation of Product Weight Percent

Weight percent of the known products from the reaction were calculated by using the relative response technique for the GC FID. Relative response factor (F$_R$) is defined by[50] :

$$F_R = \frac{A_{ref} \times W_{comp}}{A_{comp} \times W_{ref}} \tag{3.5}$$

Where A is the percentage of total area and W is the weight percentage for the component (comp) and reference component (ref). By definition Equation 3.5 is based on a response factor of 1 for the reference compound. On this basis, the numerical value of the relative response factor is the weight of the component necessary to produce the same response (area) as the reference component. The reciprocal of the relative response factor is the relative sensitivity of the FID to equal weights of the component and standard[50]. Weight percent of each product is calculated by:

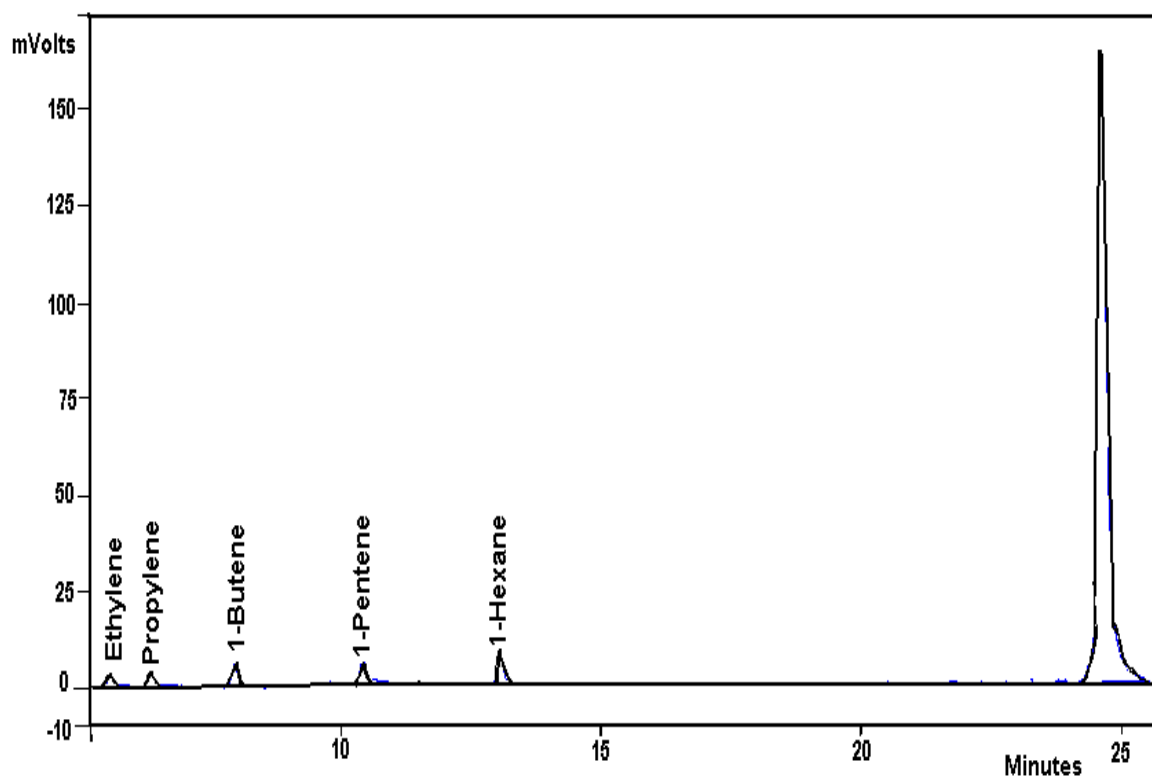$$\text{Product Weight \%} = \frac{A_x/F_{Rx}}{\sum(A_x/F_{Rx})} \tag{3.6}$$

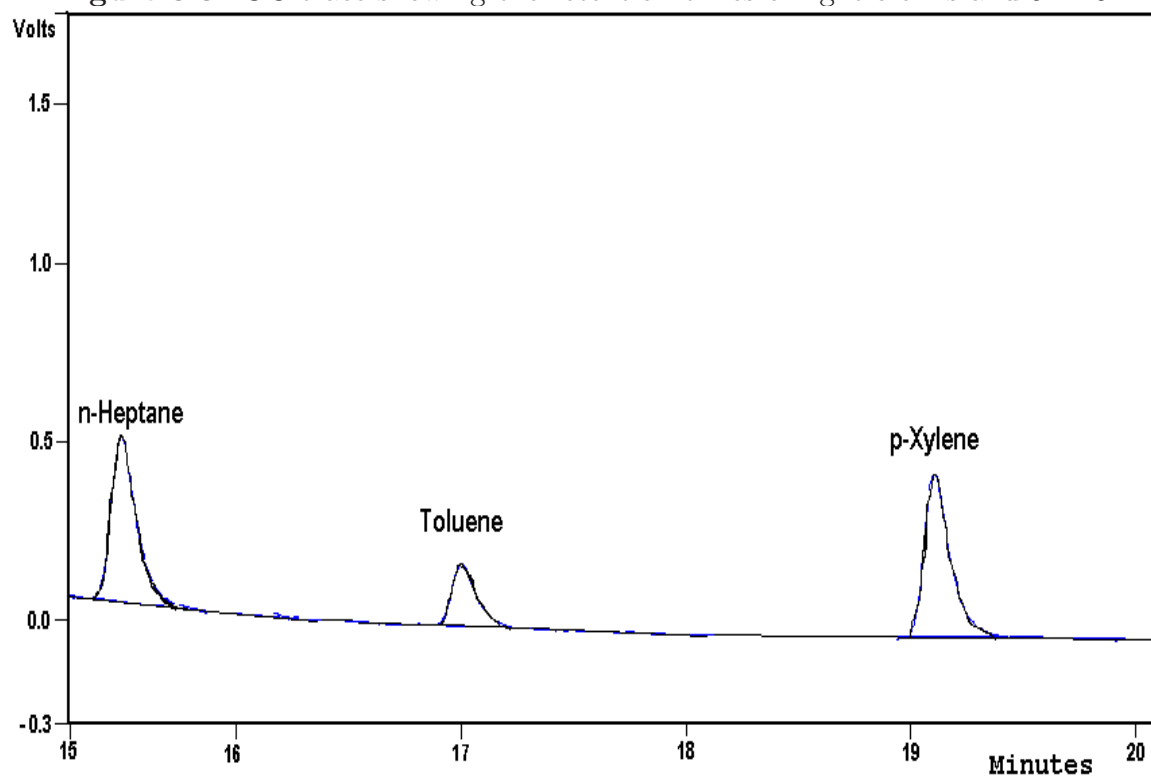**Figure 3.3** GC trace showing the retention times of light olefins and JP-10.

Figure 3.4 GC trace showing the retention times of n-hexane, toluene, and p-xylene.

The catalytic cracking reactions of JP-10 yielded over thirty different species, many of which were isomers that could not be clearly identified due to their close elution times, rendering it impossible to calculate relative response factors for every product. Response factors for the clearly identified products were calculated experimentally by injecting standards: light alkane (C to C_6) gas mixture standardized to 1,000 PPM in a balance of helium; light alkene mixture (C to C_6) standardized to 100 ppm in a balance of helium; gas mixture standardized to 100 ppm of benzene in a balance of air; and liquid solutions of 1000 ppm toluene and p-xylene, and solutions of 500 ppm of m- & o-xylenes in hexane. The three standardized gases were provided by Scott Specialty Gases.

A comparison of calculated response factors and their equivalent literature values for FID are shown in Table 3.3. 1-Butene was used as the reference component. The fact that all F_R values for hydrocarbons were close to 1.0 when using FID as the analysis technique[51]. This is demonstrated by taking the average of all the relative responses for each component, which is 0.97 and 1.01 for the experimental and reference values, respectively.

Table 3.3 Comparison of experimental relative response factors (Exp F_R) with literature values (Ref F_R)[51] (obtained by using 1-butene as the reference compound).

Product	Exp F_R	Ref F_R
Methane	0.87	0.97
Ethane	0.90	0.97
Propane	0.91	0.98
n-Butane	0.86	1.03
Pentane	0.97	1.04
Hexane	1.15	1.03
Ethylene	1.09	1.02
Propylene	1.05	1.00
1-Butene	1.00	1.00
1-Pentene	0.85	1.00
1-Hexene	0.98	0.99
Benzene	0.97	1.12
Toluene	0.96	1.07
m-Xylene	0.97	1.04
o-Xylene	0.96	1.02
p-Xylene	0.97	1.00
Average	**0.97**	**1.02**

During injection of the gas and liquid standards, a minimum area fluctuation of 10 % was difficult to achieve. This can be attributed to the inability of the GC to function in split-mode, which reduces the error by controlling the amount of sample

injected onto the column. Therefore, response factors from the literature[51] were used to calculate the weight % of the products to minimize error, as well as provide more response factors for products with no available standards. However, even the literature did not provide response factors for every product. The approximity to one for all values implies that for unknown response factors a factor of 1 can be used without causing major calculation errors. Therefore, a response factor of 1 was used for JP-10 and used in order to calculate the % weight conversion of JP-10, shown in Equation 3.7. The conversion of JP-10 to other products is used as a measure of catalyst performance (activity).

$$\% \text{ Weight Conversion of JP-10} \ = \ 100 \ - \ \frac{A_{JP-10}}{\sum(A_x/F_{Rx})} \tag{3.7}$$

Chapter 4

Results and Discussion

4.1 Catalyst Characterization

Catalyst formation is quite sensitive to synthesis conditions and post-synthesis treatments. For example, a subtle temperature change during the crystallization period can cause distortions in the catalyst framework structure. Therefore, catalysts had to be identified by their powder diffraction 'fingerprint'. SEM photos were taken of each catalyst to further support XRD findings and to detect amorphous impurities. Specific surface area and pore volume distribution were determined using nitrogen adsorption isotherms, and finally, catalyst acidic properties were analyzed using pyridine chemisorption and FTIR.

4.1.1 XRD

When indexing X-ray diffraction patterns peak intensities are set relative to the most intense peak, which is set to 100. In most cases, an identification of the catalyst and the main impurities can be achieved by following this procedure. If an impurity possesses at least one strong reflection located at an angle at least 2-theta from the reflection of the main phase of the desired product the impurity is detectable. XRD spectroscopy is able to detect crystalline impurities at a content as low as 2 to 3 %[42].

XRD patterns of nZSM-5(6h) and nZSM-5(24h) are presented in Figures 4.2 and 4.3, respectively. XRD spectra show that both nZSM-5 catalysts are very well crystallized. The spectra of nZSM-5(6h) and nZSM-5(24h) match the 'fingerprint' of the MFI structure of ZSM-5 (Figure 4.1)[48], but have a larger peak breadth. Peak broadening is solely ascribed to small crystallites[43]. From the Scherrer equation (Equation 2.12) the crystallite sizes were estimated from the most intense peak as 5.5 $\mathring{A}$ and 7 $\mathring{A}$ for nZSM-5(6h) and nZSM-5(24h), respectively.

It is very difficult to compare peak intensities using spectra from two different XRD diffractometers. However, for indexing purposes the intensities of the peaks are irrelevant[52]. Therefore, the peak intensity and peak characteristics discussion will be limited to the spectra obtained for the synthesized catalysts and not compared with the reference XRD. Therefore the relative crystallinities (%) of the two nZSM-5 samples were compared by summing the areas of six major diffraction peaks in the 2-theta region from 5 to 25^0[53]. The longer crystallization period of nZSM-5(24h) resulted in a 3 % higher crystallinity than nZSM-5(6h).

The XRD patterns for SAPO-5A and SAPO-5B are presented in Figures 4.5 and 4.6. The XRD spectra show that both SAPO-5s are well crystallized and are analogous with the reference XRD spectrum of SAPO-5[48] (Figure 4.4) with only a few discrepancies in peak intensities between the three spectra.

As desired, SAPO-5A & B have a larger peak breadth than those in the SAPO-5 spectrum obtained from the literature. The crystallite size was calculated for the peak with the highest sensitivity for SAPO-5A and SAPO-5B, which were 7 $\dot{A}$ and 7.5 $\dot{A}$, respectively.

The crystallinity of SAPO-5A and SAPO-5B were also compared by summing the areas of six major diffraction peaks in the 2-theta region from 5 to 25^0[53]. From this calculation, SAPO-5B is 25 % less crystalline than SAPO-5A.

SAPO-11 seemed to be the most capricious to synthesize. Synthesis was repeated three times to obtain a satisfactory crystallinity with only a small amount of impurities. SAPO-31 was also often produced during the synthesis of SAPO-11. This trend was also observed by Sinha et al.[53]. The XRD spectrum of SAPO-11 is presented in Figure 4.8. The XRD spectra shows a well crystallized catalyst with small crystallites. The strongest evidence of the small crystallites is in the area of 20 and 25 2-theta where the peaks are much wider and less defined than in the same area of the reference XRD pattern in Figure 4.7[48]. The particle size calculated for the most intense peak was 12 $\dot{A}$.

4.1.2 Scanning Electron Microscope

In Figure 4.9, nZSM-5(6h) appears to be spherical to cylindrical polycrystallites with a 10 μm average diameter. Ali et al.[54] also reported sphericle to cubicle shapes for ZSM-5, however, with only a 1 μm average diameter. The small crystalites that form the larger aggregates in Figure 4.10 have an average length between 0.2 and 0.6 μm. This trend is even more evident in nZSM-5(24h) (Figures 4.11 and 4.12) due to the longer crystallization time. The average length of the larger aggregates in nZSM-5(24h) are approximately 12 μm, and the smaller crystallites are between 0.3 and 0.7 μm.

SAPO-5A closely resembles the barrel-like growth polycrystalline aggregates reported for ALPO-5 by Concepcion et al.[55]. It is obvious from Figures 4.13 and 4.14
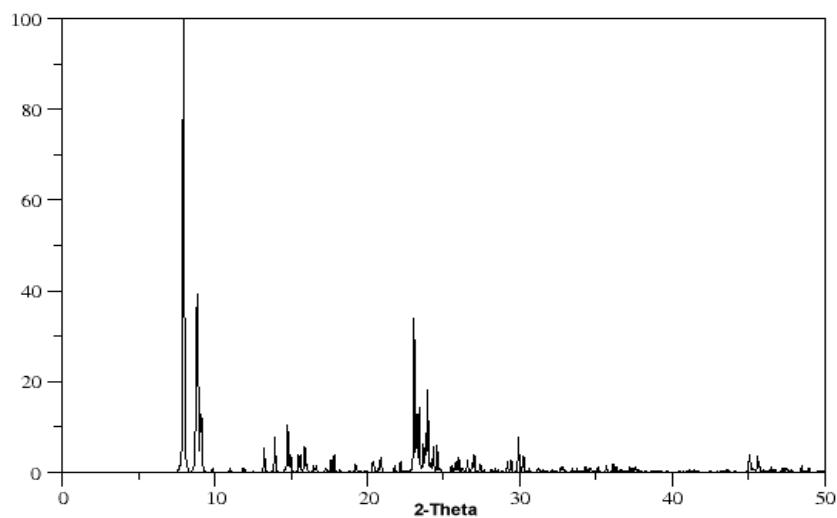
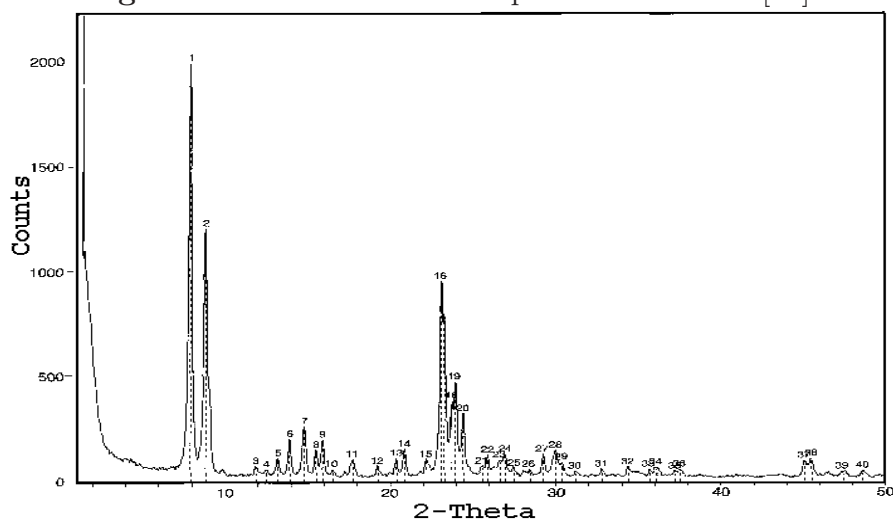**Figure 4.1** Reference XRD Spectrum of ZSM-5[48].
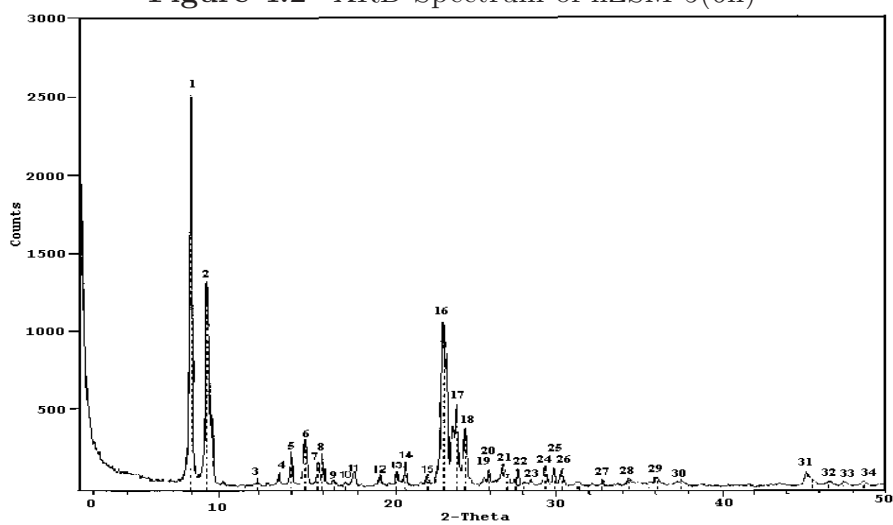

Figure 4.2 XRD Spectrum of nZSM-5(6h)

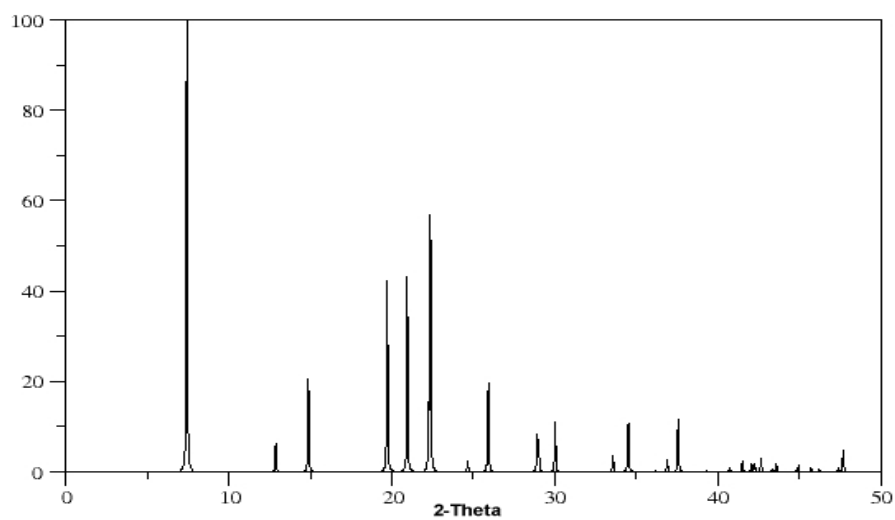**Figure 4.3** XRD Spectrum of nZSM-5(24h).

Figure 4.4 Reference XRD Spectrum of SAPO-5[48].

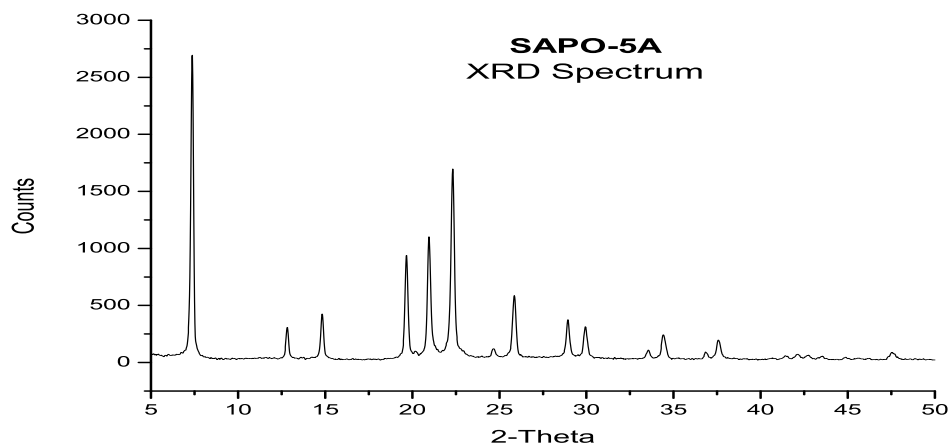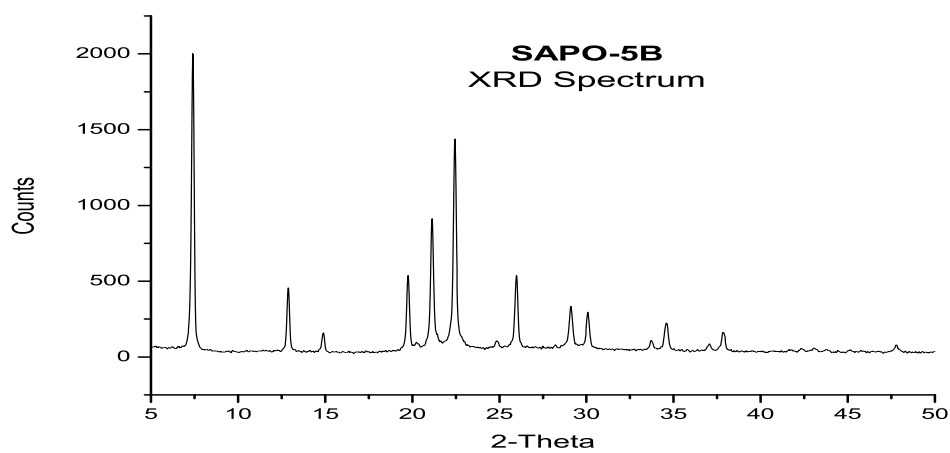**Figure 4.5** XRD Spectra of SAPO-5A.

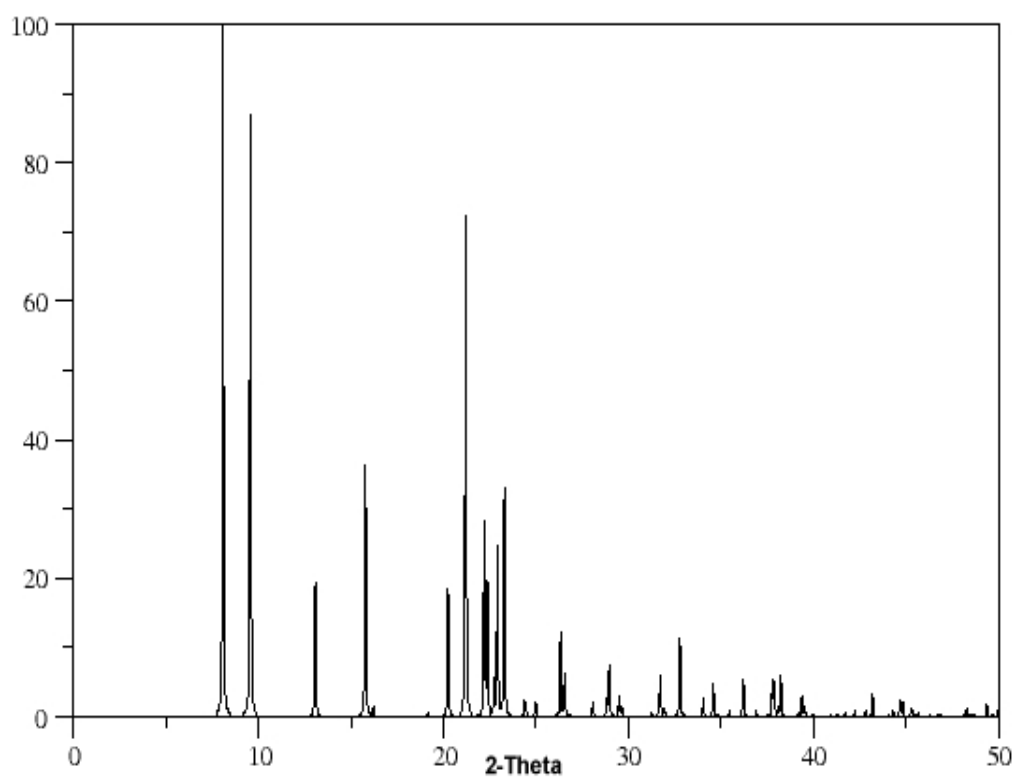**Figure 4.6** XRD Spectra of SAPO-5B.

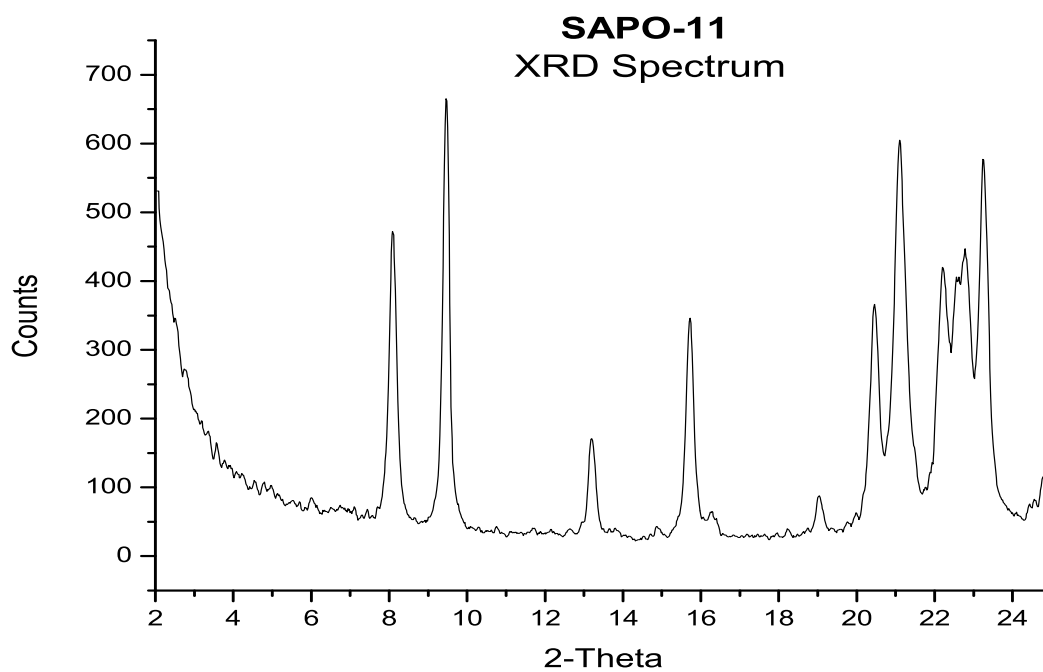**Figure 4.7** Reference XRD Spectrum of ALPO-11[48].
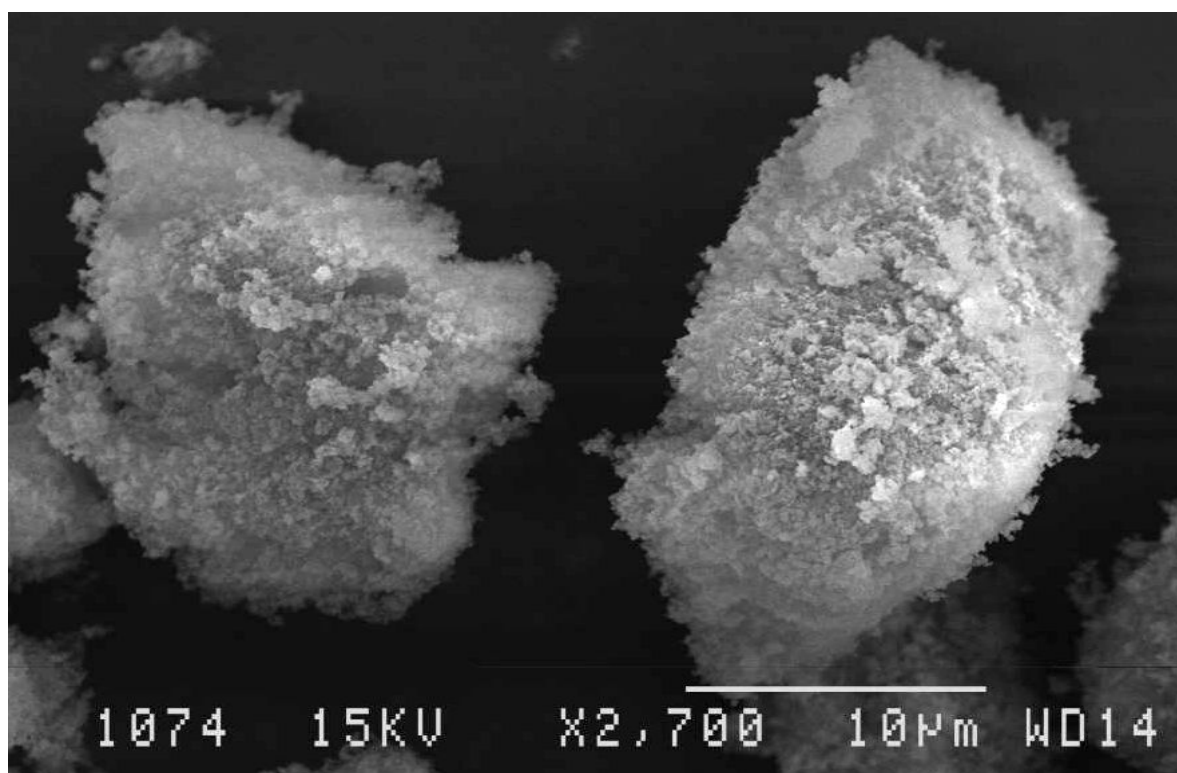

Figure 4.8 XRD Spectrum of SAPO-11.

Figure 4.9 SEM of nZSM-5(6h)
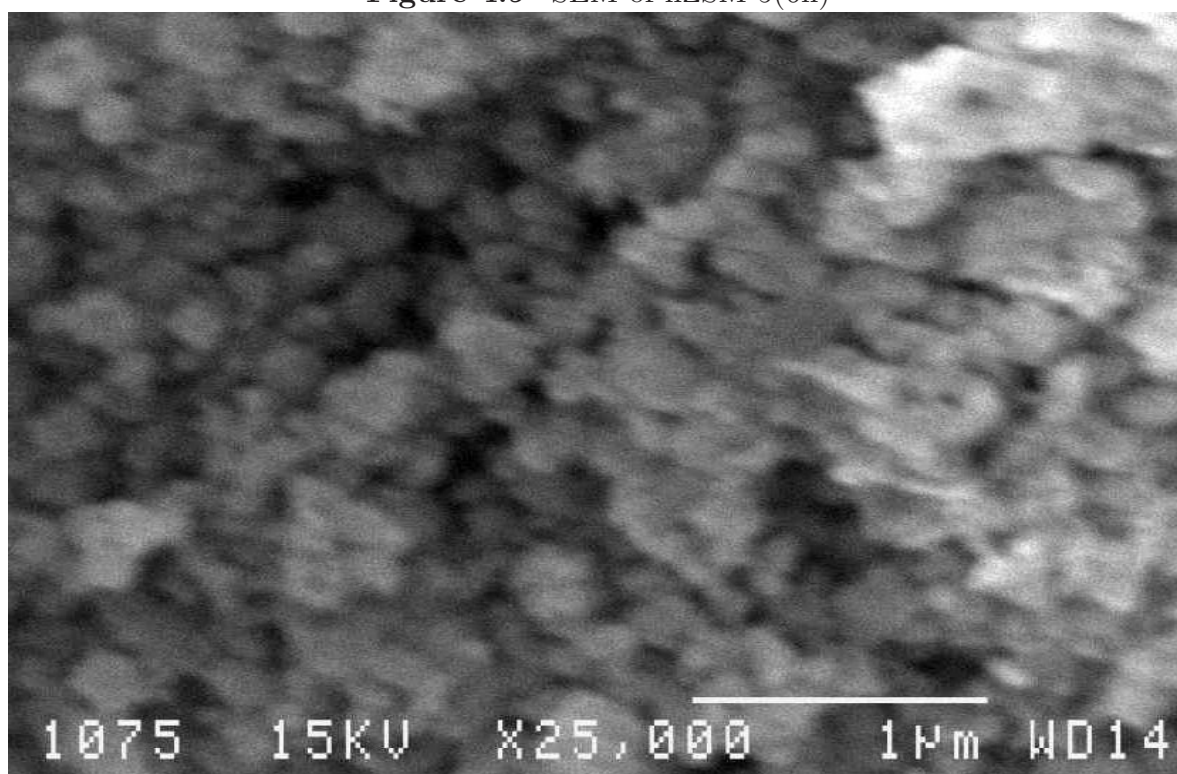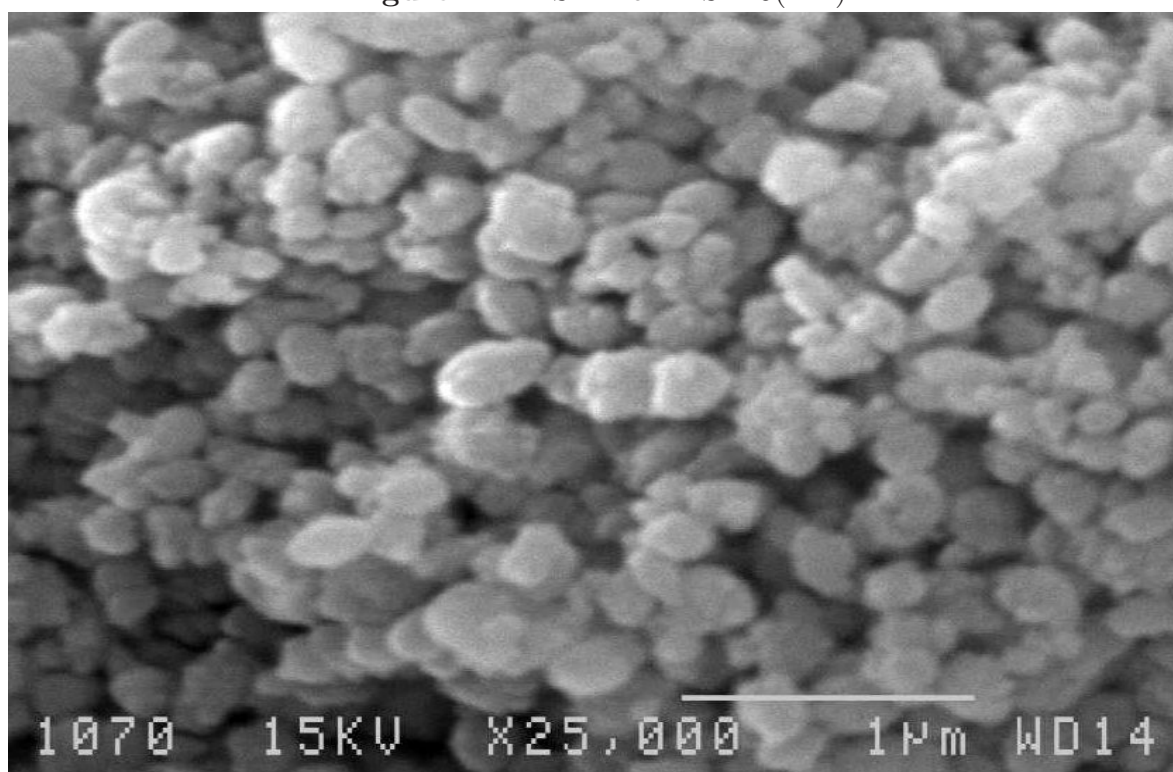

Figure 4.10 SEM of nZSM-5(6h)
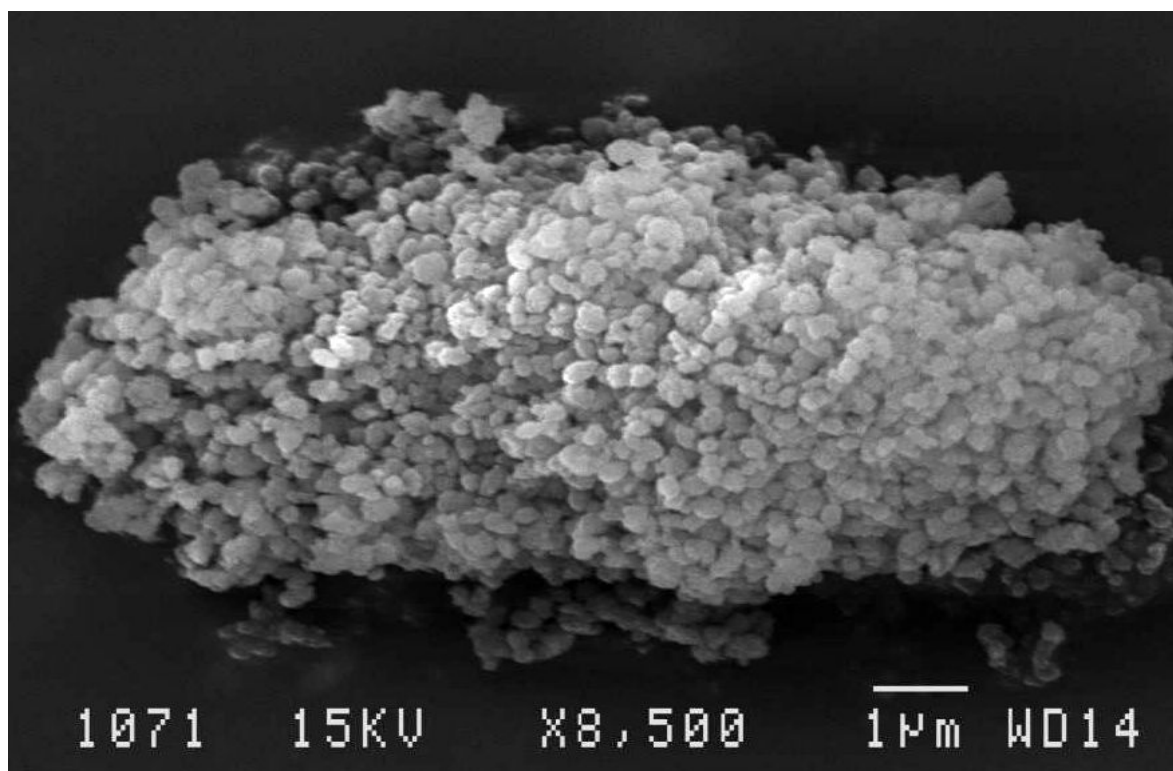
Figure 4.11 SEM of nZSM-5(24h)

Figure 4.12 SEM of nZSM-5(24h)

that the aggregates of SAPO-5A are hollow with two different size exits. The end exits are the largest with an average diameter of 5 μm and the smaller side exit has an average diameter of 2 μm.

SAPO-5B does not follow the same trend as SAPO-5A. As seen in Figure 4.15, SAPO-5B resembles the hexaganol plates reported by Wang et al.[56] for high silica SAPO-5 (0.25 and 0.42 Si:Al). However, there does appear to be some barrel-like growth polycrystalline impurities in SAPO-5B, but are approximately less than one half the size of those reported for SAPO-5A. It is not surprising to see both forms of SAPO-5 together as they were synthesized in the same batch.

The average diameters of SAPO-5A and SAPO-5B are 10 μm and 5 μm, respectively. This size difference between the two SAPOs are expected, because the larger, heavier crystals of SAPO-5A were collected by decanting, whereas the smaller, lighter crystals of SAPO-5B had to be separated by centrifugation.

The ball shaped aggregates for SAPO-11, shown in Figure 4.16, has also been reported for SAPO-11 by Sinha and Seelan[53]. The average diameter of the ball-like crystallites are 3 to 5 μm. It is not surprising that Figures 4.17 and 4.17 show that there are extensive needle-like shape impurities that resembles the structure reported for SAPO-31[53]. The synthesis method of SAPO-31 closely resembles that of SAPO-11 and it is not surprising that these two catalyst form together.

4.1.3 Nitrogen Adsorption Isotherms

The specific surface areas of the catalysts were calculated by applying the BET equation to N_2 adsorption t-plot isotherms in the relative vapour pressure (P/P$_o$) range 0 to 0.1, which is the surface area based on the linear portion of the BET plot. The catalyst specific surface areas are given in Table 4.1.

The highest specific surface areas calculated were 385 m^2/g and 427 m^2/g for nZSM-5(6h) and nZSM-5(24h), respectively. These agree with the specific surface area for nZSM-5 crystallized for 72 h (438 m^2/g) reported by Serrano et al.[39].

Wang et al.[56] reported a surface area for SAPO-5 with Si/Al of 0.25 is 359 m^2/g, while it decreases sharply to 267 m^2/g at Si/Al ratio of 0.42. This implies that the 217 m^2/g and 216 m^2/g surface areas achieved in this study for SAPO-5A and SAPO-5B with a Si/Al ratio of 0.33 are as expected.

The specific surface areas of both SAPO-5 and SAPO-11, however, are much higher than those reported for catalysts subjected to longer crystallization at higher temperatures[57]. A difference in Si/Al ratio would also have a significant effect on specific surface area and catalyst acidity[56].

Adsorption isotherm curves for nZSM-5(24h) and SAPO-5B are given in Figures 4.19 and 4.20, respectively. These are typical physisorption isotherms that are exhibited by
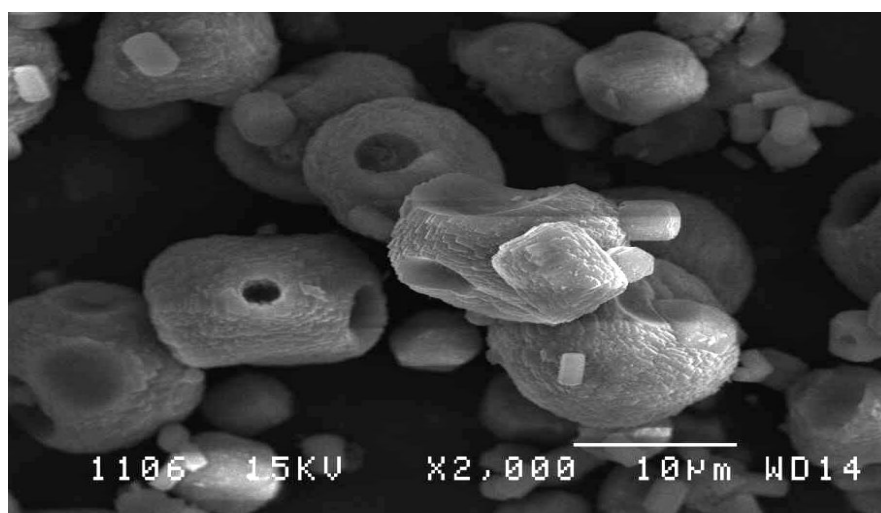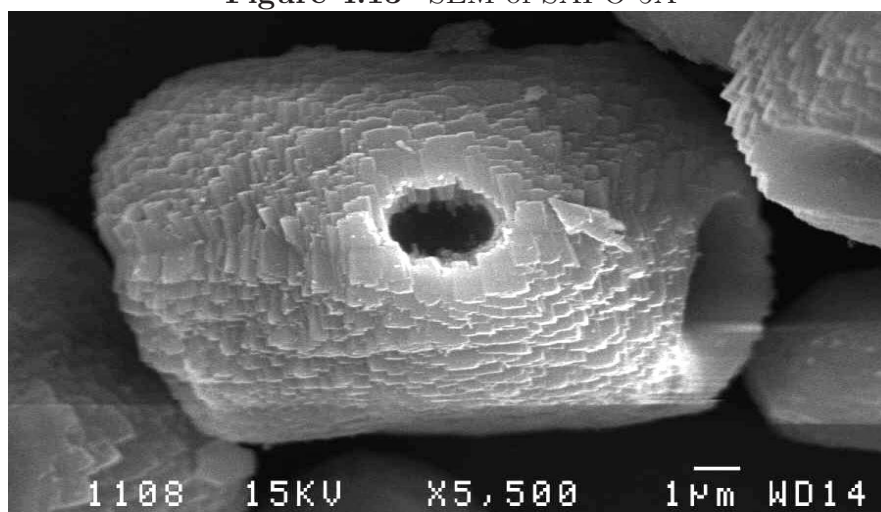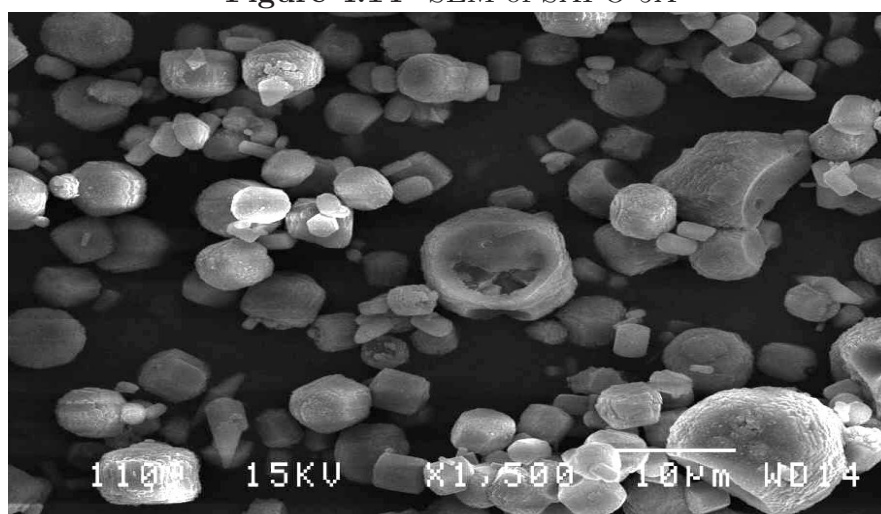
Figure 4.13 SEM of SAPO-5A

Figure 4.14 SEM of SAPO-5A
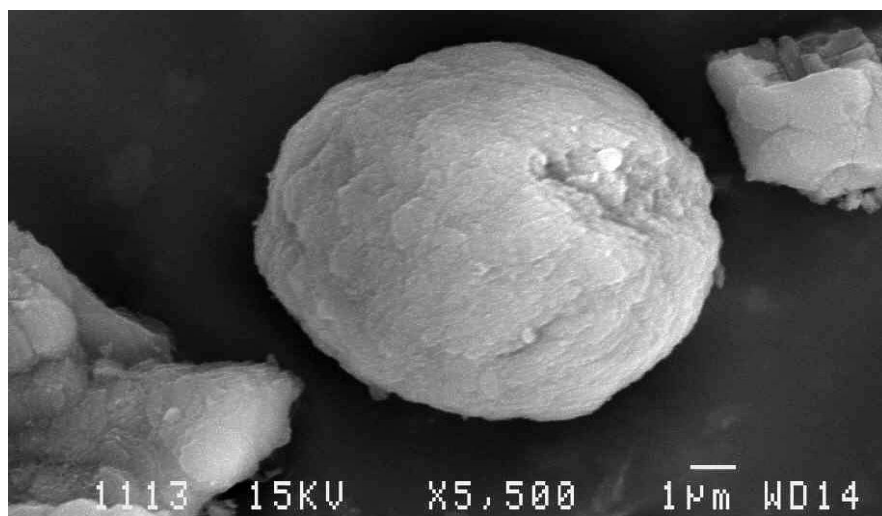

Figure 4.15 SEM of SAPO-5B
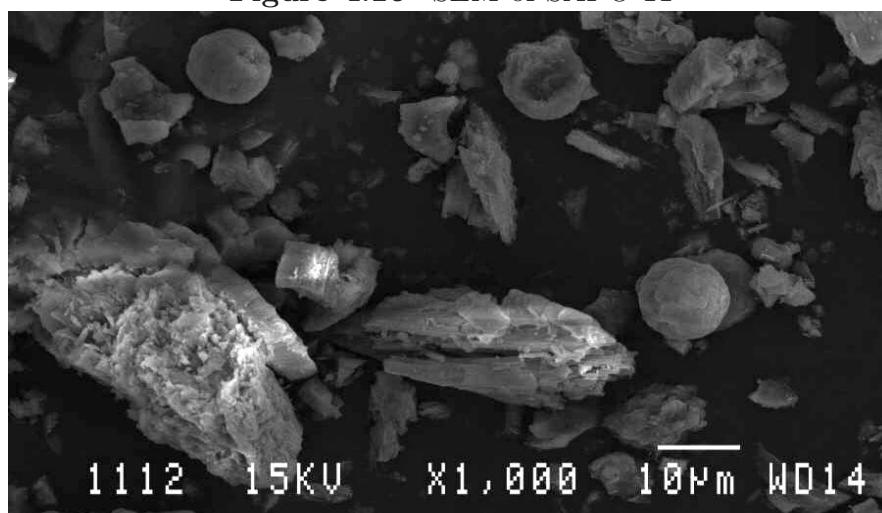
Figure 4.16 SEM of SAPO-11
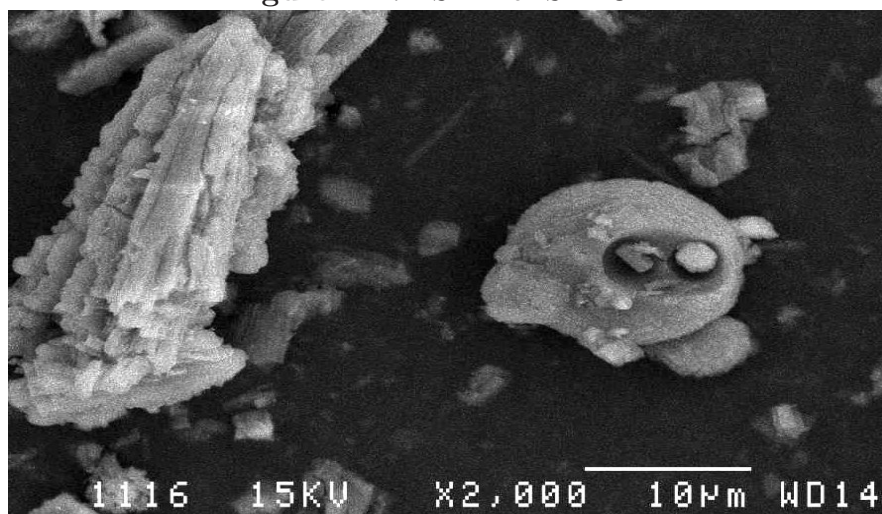

Figure 4.17 SEM of SAPO-11
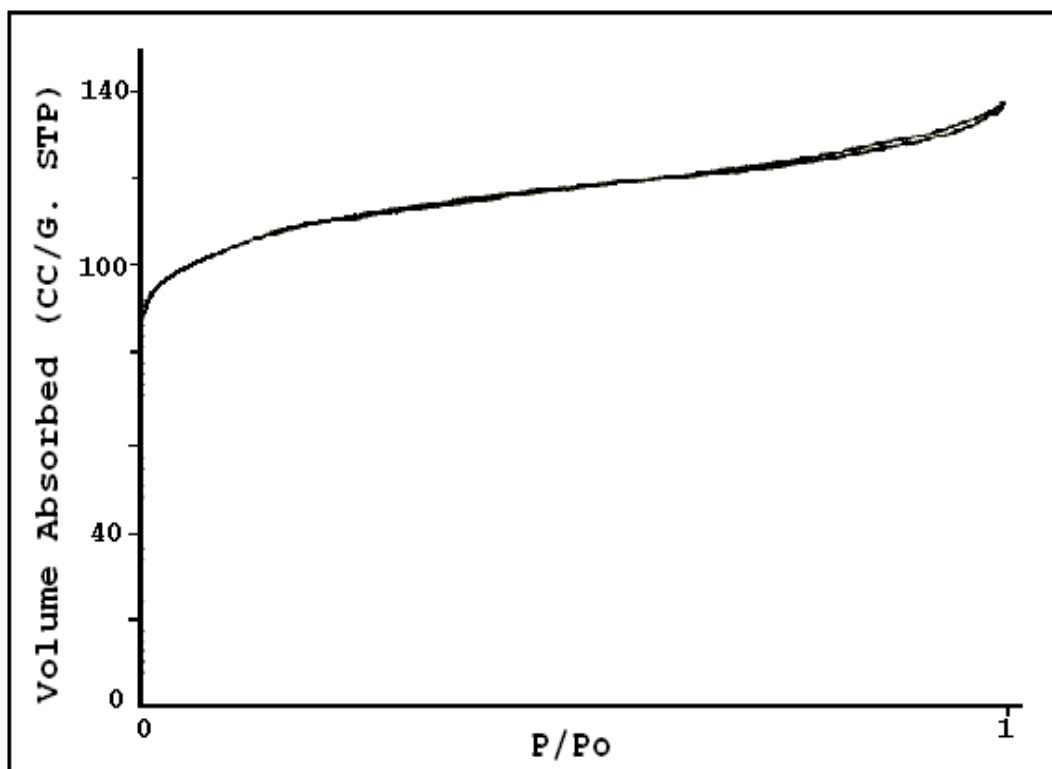

Figure 4.18 SEM of SAPO-11

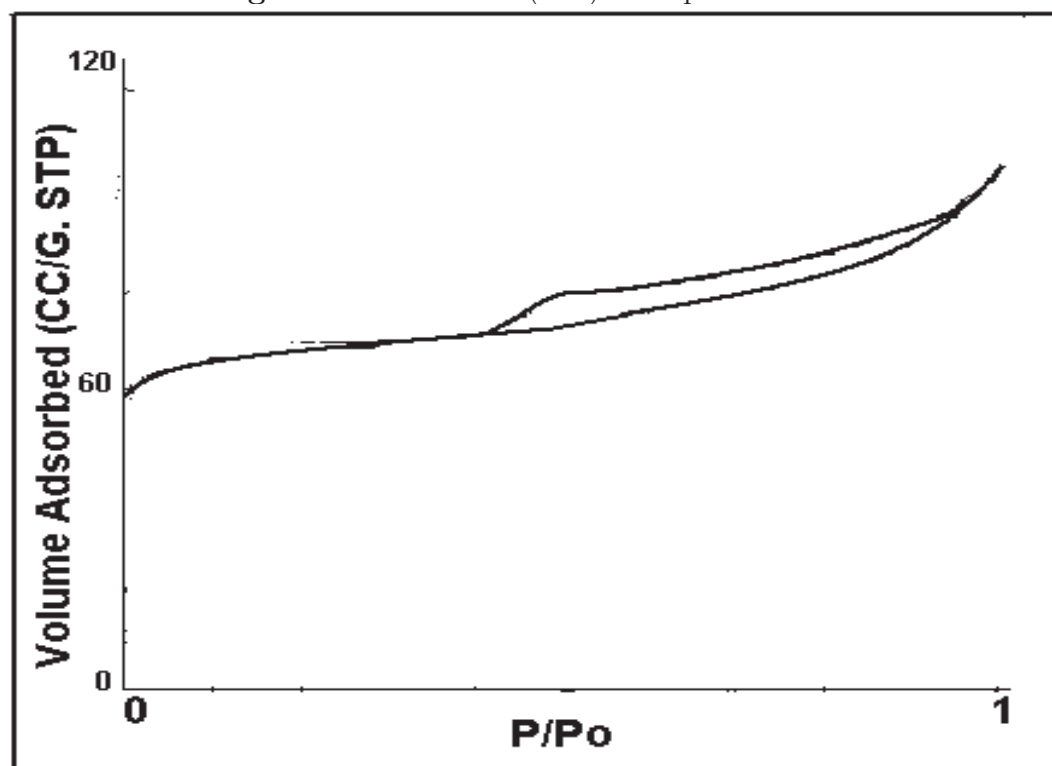**Figure 4.19** nZSM-5(24h) adsorption isotherm curve.

Figure 4.20 SAPO-5B adsorption isotherm curve.

Table 4.1 BET of catalysts

Catalyst	Specific Surface Area (m^2/g)	Micropore Vol. (ml/g)	Meso & Macropore Vol. (m^2/g)
nZSM-5(6h)	385	0.15	76
nZSM-5(24h)	427	0.14	74
SAPO-5A	263	0.09	46
SAPO-5B	262	0.09	43
SAPO-11	191	0.06	37

microporous solids having relatively small external surfaces. The limiting uptake of adsorbate is governed by the accessible micropore volume rather than by the internal surface area. Using the deBoer classification, the BET method for determining the specific surface area generally applies to type II isotherms characteristic of non porous solids. However, it is possible to apply the type IV isotherm to catalysts characteristic of mesoporous solids if the region before the hysterisis is similar to that of type II[44].
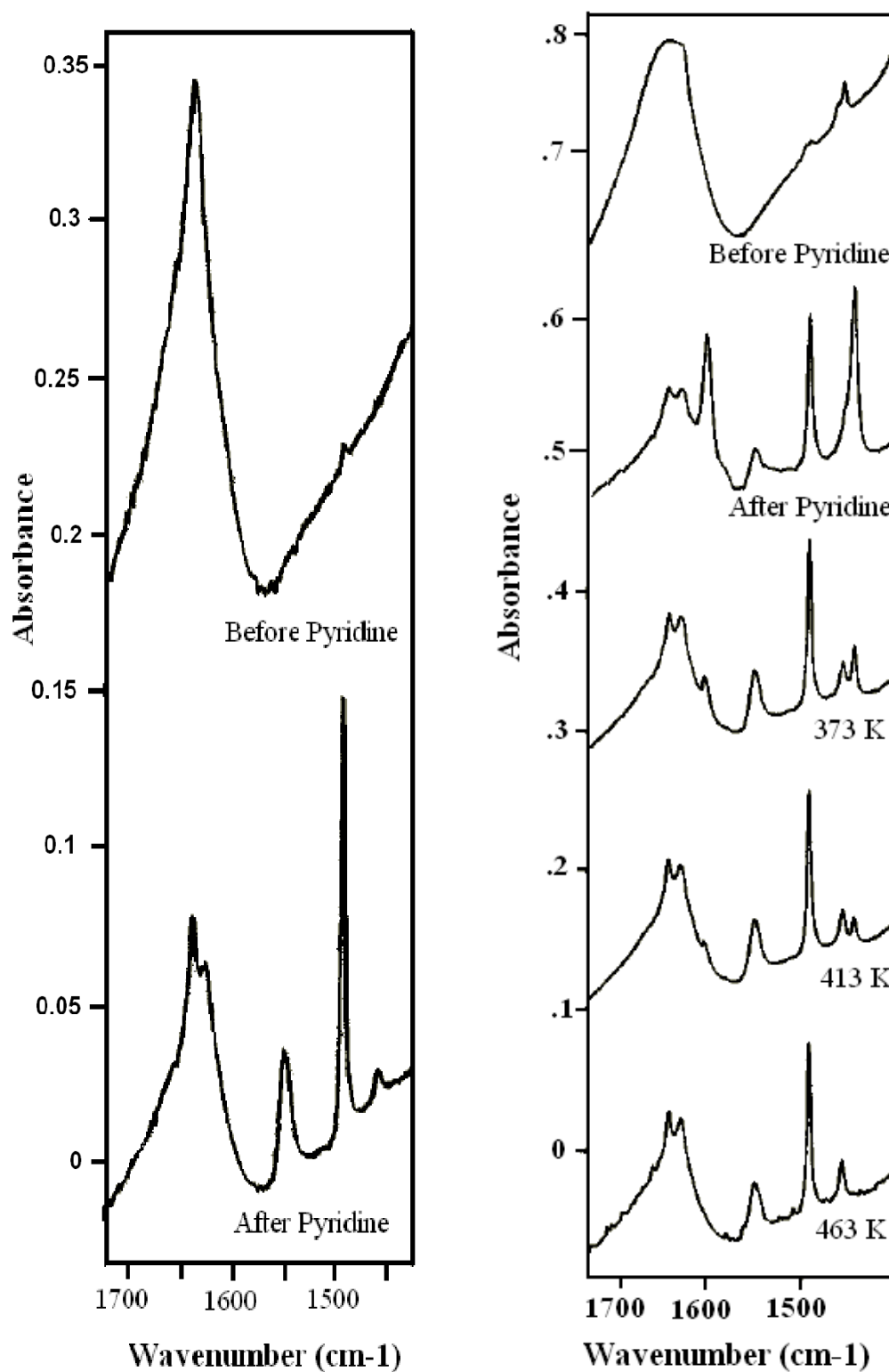
4.1.4 Pyridine Chemisorption

The acid site density was obtained by using Fourier Transform-infrared (FTIR) spectroscopy of the catalyst before chemisorption of pyridine and after chemisorption of pyridine. The before and after FTIR spectra for nZSM-5(6h), nZSM-5(24h), SAPO-5A and SAPO-11 are shown in Figures 4.21 and 4.22.

These spectra show the appearance of different absorption bands corresponding to the chemisorption of pyridine on the catalysts' acidic sites. The 'before pyridine' spectra essentially show no peaks in the 1425-1575 cm^{-1} range, except for one very minor peak at 1450 cm^{-1}.

The spectra designated as 'after pyridine' were recorded at room temperature. They show a peak at 1610 cm^{-1} that is assigned to Lewis acid sites. The peak at 1490 cm^{-1} is assigned to both Lewis and Bronsted acid sites[49, 58, 59]. The broader 1450 cm^{-1} peak may be due to some residual chemisorbed pyridine, which would, however, not contribute to the 1490 cm^{-1} peak[49]. The 1638 cm^{-1} and 1550 cm^{-1} peaks are assigned to Bronsted acid sites[49, 58, 59].

SAPO-5 and nZSM-5(24h) show the strongest peaks at 1610 cm^{-1} Lewis acid sites, suggesting these two catalysts have the highest density of available surface sites compared to the other catalysts. SAPO-11 has the strongest peak at the 1550 cm^{-1} Bronsted band. This agrees with the findings that SAPO-11 has a larger poor size and surface area compared to all of the other catalysts.

Figure 4.21   FTIR spectra of pyridine chemisorbed on nZSM-5(6h) (left) and nZSM-5(24h) (right).
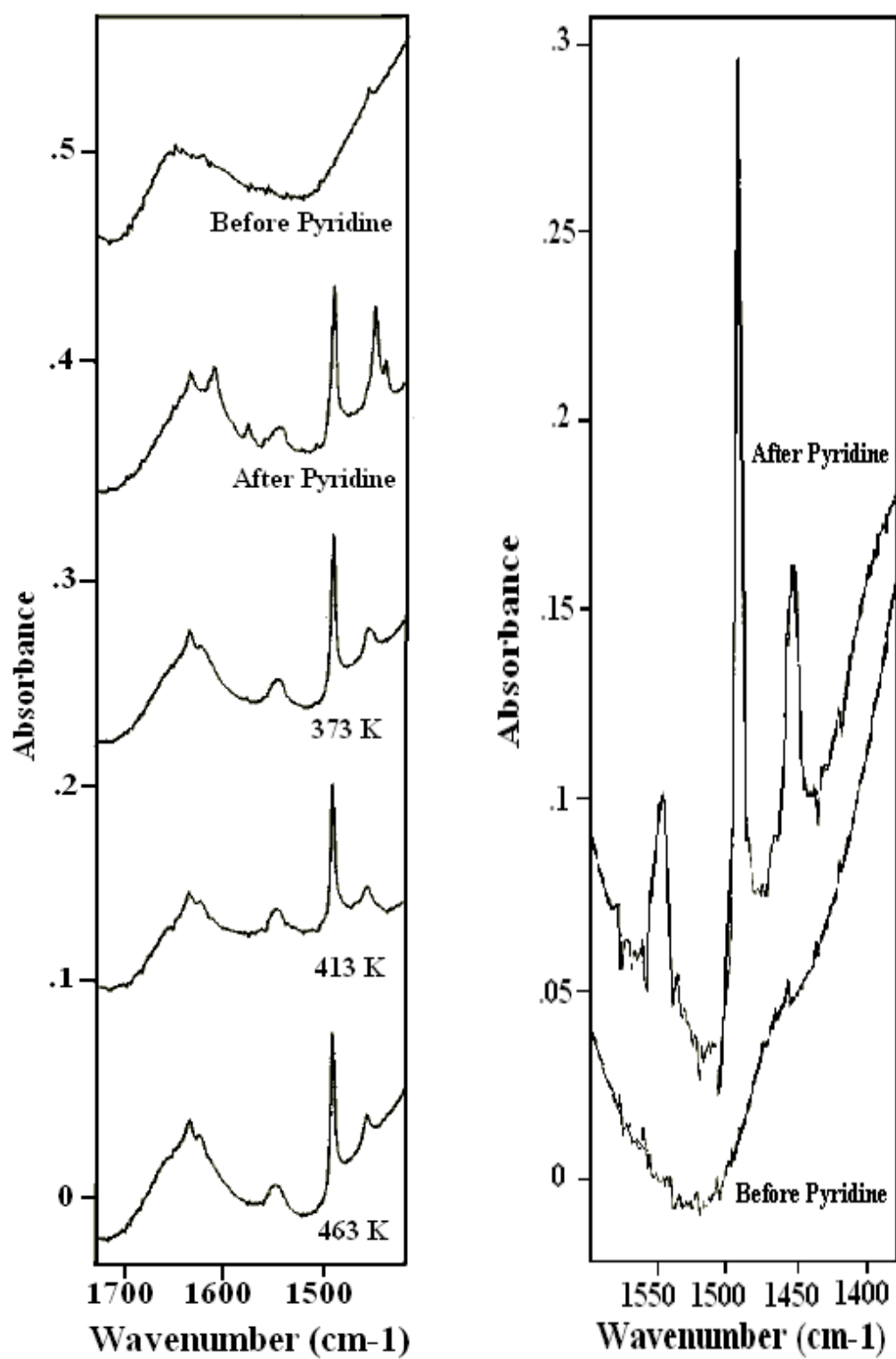
Figure 4.22 FTIR spectra of pyridine chemisorbed on SAPO-5A (left) and SAPO-11 (right).

4.2   Nanocrystalline ZSM-5 Activity

In this study, activity is used as a measure of catalyst performance. It is defined as the % conversion of JP-10 to other products. Figure 4.23 compares the activity of nZSM-5(6h) and nZSM-5(24h) versus reaction temperature. Two tests for nZSM-5(24h) were carried out by leaving the catalyst from the first test in the reactor. The catalyst was reconditioned for the second test by flowing an air/helium gas mixture through the reactor for approximately 5 h at 550 ^{o}C.
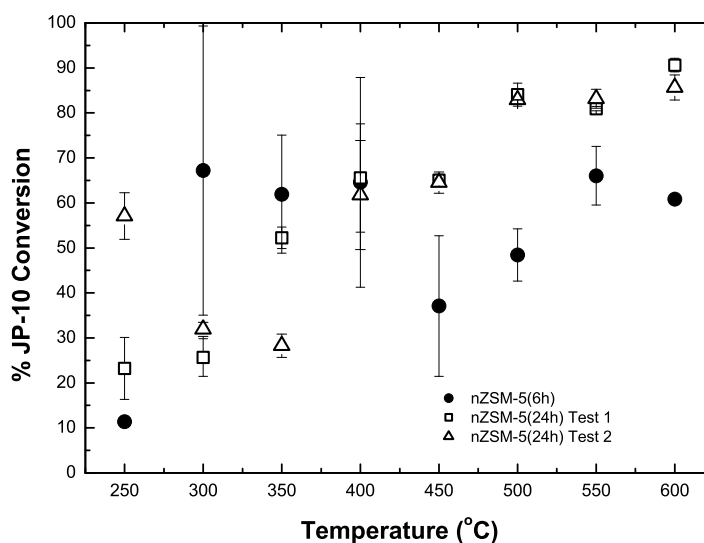
Figure 4.23 % JP-10 conversion over nZSM-5(6h) and nZSM-5(24h) versus reaction temperature (65 h WHSV).

As expected, the activity of nZSM-5(24h) increased with temperature; however, nZSM-5(6h) did not seem to follow a similar pattern. nZSM-5(6h) actually showed the highest activity between 300 ^{o}C and 400 ^{o}C. After 400 ^{o}C the activity falls dramatically and high conversion rates are only again achieved at 550 ^{o}C and higher. nZSM-5(24h) did not match the highest % JP-10 conversion of nZSM-5(6h) until 400 ^{o}C; however, at temperatures higher than 400 ^{o}C, the activity of nZSM-5(24h) continued to increase, reaching 90 % conversion.

Although nZSM-5(24h) was reconditioned before the second test, this process would not likely have been sufficient enough to remove all of the coke deposits formed on the catalyst surface. Therefore, the high activity level of the second test indicates nZSM-5(24h) has a high tolerance for coking. The second test actually surpasses the activity level of the first test at 250 ^{o}C and 300 ^{o}C. There is a drop in activity at 350 ^{o}C, but

the second test activity matches that of the first test at temperatures above 400 ^{o}C. This trend was also observed by Serrano et al.[39]

Carbon ratio (CR) is defined as the ratio of the weight % of all gaseous products having carbon chains of C_5 and longer divided by the weight % of all products having chains of C_4 and shorter. Theoretically, small carbon products will cause less coking and in general, will be easier to detonate. Therefore, a lower CR suggests a more desirable mixture of products for detonation applications.

The major fault with this method of product comparison is it does not distinguish between alkanes, alkenes, nor aromatics. As previously mentioned, propane is the most undesired light hydrocarbon as it holds very similar detonation properties to JP-10. There was no evidence of propane during GC/MS analysis. Most C_3 products were identified as propene or one of it isomers. Therefore, it is highly likely that most of the light hydrocarbons are indeed the desired alkenes and their isomers and not alkanes. Therefore, in this study CR is considered an acceptable method to be used for catalyst comparison. The CR provides a quantitative indication of the amount of desired short chain hydrocarbons to undesirable large hydrocarbons.

Thus, the objective of this study is to achieve the lowest possible CR with the highest conversion rate. However, this is not as evident as it seems. A high % conversion creates an environment more prone to secondary reactions, like cyclization, which forms undesirable products like aromatics. Therefore, to reduce secondary reactions it is also important to consider all the factors that effect the rate of secondary reactions, like temperature, space velocity (WHSV), and acidity

The CR versus reaction temperature for nZSM-5(6h) and nZSM-5(24h) is shown in Figure 4.24. The lowest CR is produced with nZSM-5(24h) between 350 ^{o}C and 450 ^{o}C. This corresponds to the 50 to 70 % conversion range, as presented in Figure 4.25. CR values for nZSM-5(6h) are much higher than nZSM-5(24h). This is most likely due to the higher acidic properties of nZSM-5(6h), because a high acidic environment promotes secondary reactions.

4.3 SAPO Activity

Both forms of SAPO-5 show great potential for the catalytic cracking of JP-10. Due to the initial success with SAPO-5B, less catalyst (25 mg) was used in the first test using SAPO-5A. As with nZSM-5(24h), the catalyst was left in the reactor after the first test and reconditioned with an air/helium flow for approximately 5 h at 550 ^{o}C. As shown in Figure 4.26, SAPO-5A did not match the constant high activity level of SAPO-5B; therefore, 50 mg of fresh catalyst was used in the SAPO-5A third test.

The decreased WHSV in the SAPO-5A third reaction slightly raised the average conversion from 31 % to 33 % and decreased the CR from 2.6 to 2.3 (presented in Ta-
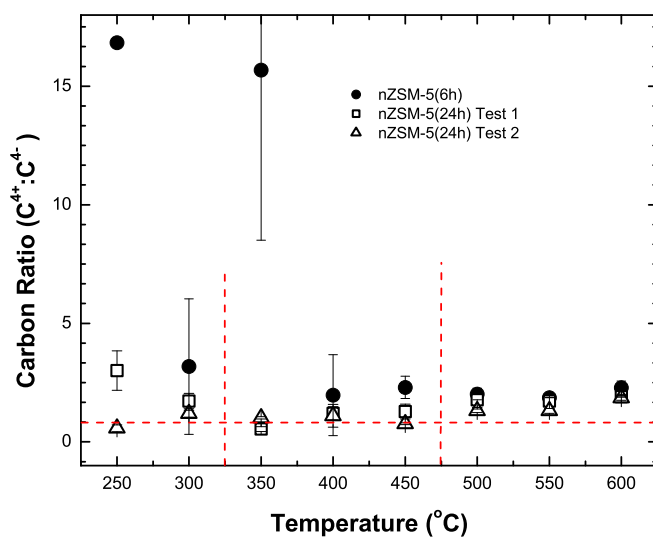
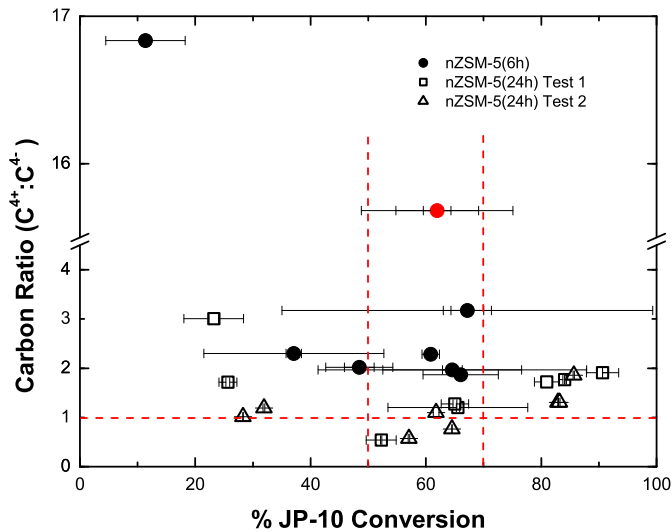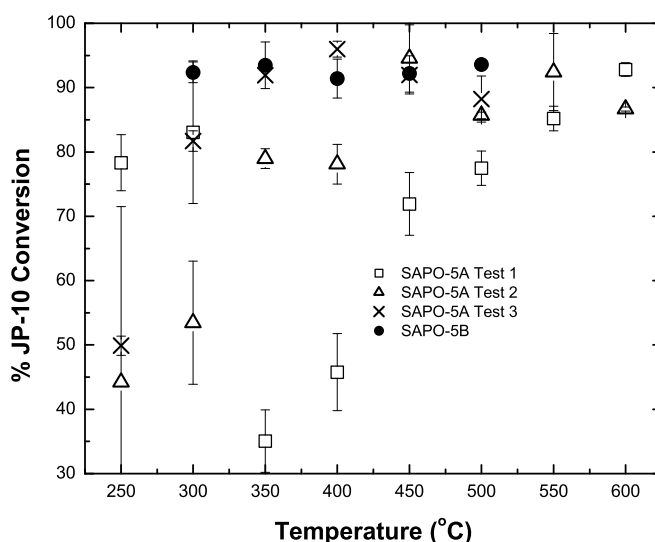**Figure 4.24** CR versus reaction temperature for nZSM-5(6h) and nZSM-5(24h).

Figure 4.25 CR versus % JP-10 conversion by nZSM-5(6h) and nZSM-5(24h).

ble 4.2). Both forms of SAPO-5 achieved over 90 % conversion of JP-10 between 300 ^{o}C and 600 ^{o}C. SAPO-5B had a consistently high conversion rate ($\approx$ 90 %) throughout the reaction temperature range.

The activity in the third test of SAPO-5A peaked at the lower temperatures 350 ^{o}C and 450 ^{o}C. The lowest CR values are identified in Figures 4.27 and 4.28 as being at 450 ^{o}C and 500 ^{o}C, corresponding to 75 % and 90 % JP-10 conversion. The less acidic environment of SAPO-5 provides less of a platform for secondary reactions to occur. Thus, higher conversion does not necessarily mean an increased CR. SAPO-5B has the lowest average CR, but at 450 ^{o}C and 500 ^{o}C, the first and second tests of SAPO-5A yielded the lowest CR. This is expected as the reactant has less time on contact with the catalyst, reducing the chance of secondary reactions to occur.

SAPO-5A does not seem to have a high tolerance to coking. The drop in activity at 350 ^{o}C and 400 ^{o}C in the first test and the reduced activity in the second test suggests that the catalytic reaction becomes more dependent on the temperature increase as coke builds up.

Figure 4.26 % JP-10 conversion by SAPO-5A 1st and 2nd test (68 h and 85 h WHSV, respectively) and SAPO-5B (75 h WHSV) versus reaction temperature.

SAPO-11 performed poorly compared to the other catalysts. The % JP-10 conversion follows a linear trend as the temperature increases in the SAPO-11 tests (see Figure 4.29). High % conversion is only achieved above 500 ^{o}C. As shown in Figures 4.30 and 4.31, SAPO-11 achieves the lowest CR at 400 ^{o}C and 450 ^{o}C, corresponding to conversions between 30 % and 50 %.
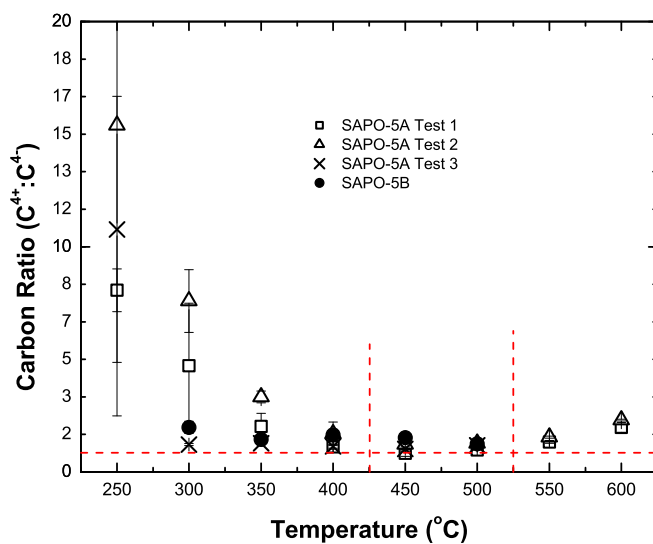
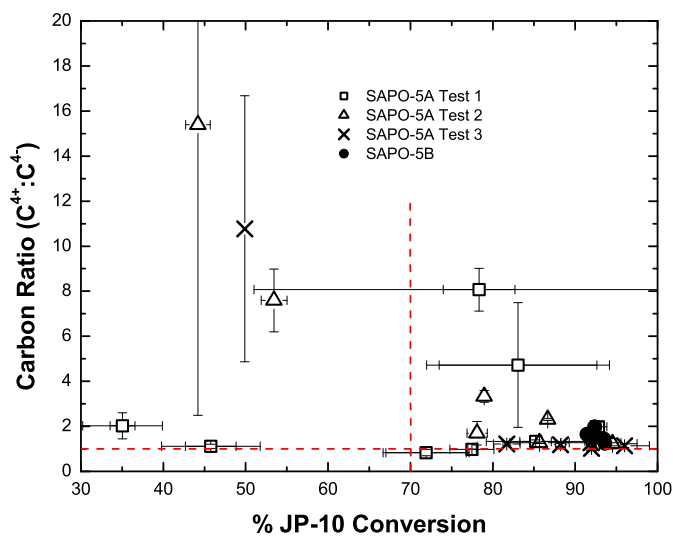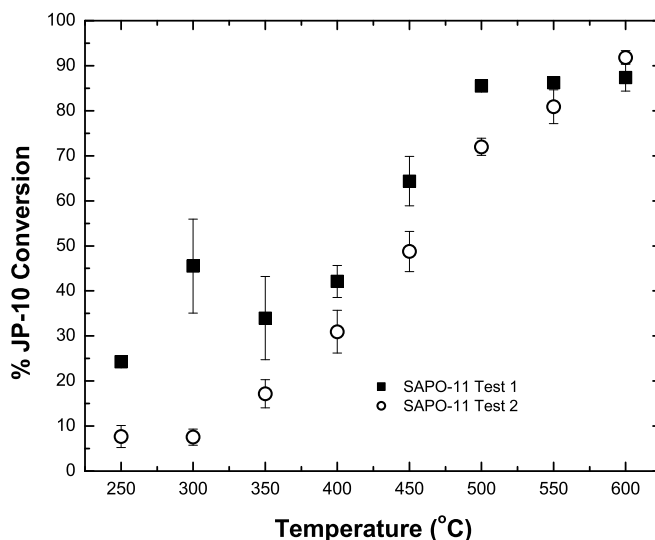**Figure 4.27** CR versus reaction temperature for SAPO-5A & B.

Figure 4.28 CR versus % JP-10 conversion by SAPO-5A & B.

Figure 4.29 % JP-10 conversion by SAPO-11 versus reaction temperature (63 h WHSV).

4.4   General discussion

Table 4.2 shows the average CR and average conversion of JP-10 over the entire temperature range for each catalyst test. This provides a general indication of which catalyst test resulted in the highest conversion rate with the lowest CR. The second test of nZSM-5(24h) had the highest activity of the zeolites with a 75 % lower CR than the first nZSM-5(24h) test. Whereas both SAPO-5 samples show a lower CR during the first tests when there has been less time for coke deposits to form. However, overall, SAPO-5B had the lowest CR with the highest conversion overall. This suggests that highly crystalline SAPO-5 is an ideal catalyst for short flight applications where coking is not a major factor and nZSM-5(24h) is more suited for longer flight applications where coking must be considered. SAPO-11 demonstrates the lowest average activity and slighlty higher CR averages compared to the other catalysts. Therefore, SAPO-11 is not an ideal candidate for catalytic cracking in detonation applications.

For this study, it is necessary to determine the catalyst properties that had the most influence during the cracking of JP-10. Two factors that seem to have great significance in obtaining the desired light olefin mixture are the abundance of active surface sites and the high density of Bronsted acid sites. This claim can be substantiated by comparing the low activity and the higher than average CR of SAPO-11 to the two most promising catalysts, SAPO-5B and nZSM-5(24h) (see Table 4.2). Pyridine chemisorption on SAPO-11 showed very low Bronsted site density, but very high Lewis
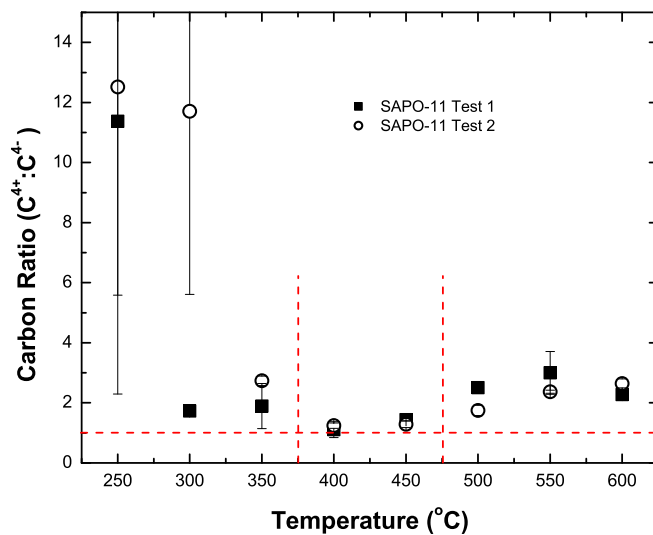
Figure 4.30 CR versus reaction temperature for SAPO-11.
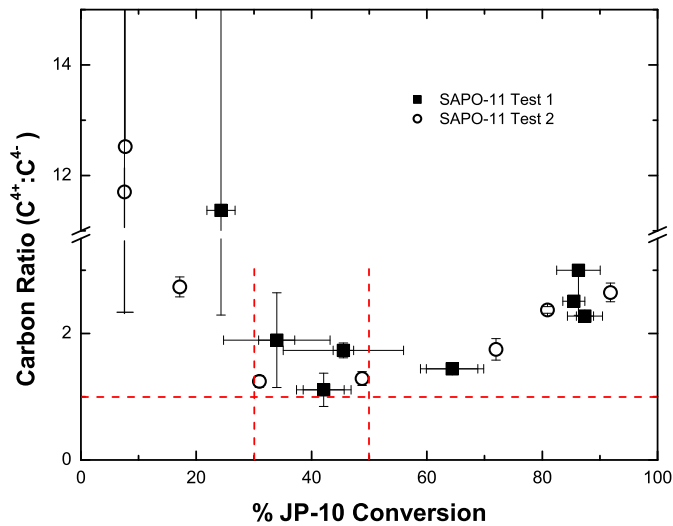
Figure 4.31 CR versus % JP-10 conversion by SAPO-11.

Table 4.2 The average CR and % conversion throughout the temperature range of each test.

Catalyst	Average CR	Average % Conversion
nZSM-5(6h)	4.9	57.2
nZSM-5(24h) 1st test	4.3	65.8
nZSM-5(24h) 2nd test	1.3	67.9
SAPO-5A 1st test	2.6	71.2
SAPO-5A 2nd test	4.3	76.8
SAPO-5A Repeat	2.3	85.9
SAPO-5B	1.6	88.6
SAPO-11 1st test	2.0	59.2
SAPO-11 2nd test	4.5	44.6

acid site density. Whereas both SAPO-5B and nZSM-5(24h) had very high Bronsted site density. SAPO-11 also had the lowest surface area (191 m^2/g) and thus, the largest poor size (12 $\dot{A}$) compared to all of the other catalysts.

Chapter 5

Conclusion

The attempt to reduce the crystal size of SAPO-5 and SAPO-11 was successful. Evidence of small crystallites from peak broadening on the XRD spectra was confirmed by the SEM photographs. The crystalline size of nZSM-5 estimated by using the Scherrer equation on the XRD spectra and from direct measurement on the SEM photographs were between the expected range 10 and 100 nm. Shorter crystallization periods for nZSM-5 would more than likely produce smaller pore sizes.

Among the solids examined in this study, SAPO-5B and nZSM-5(24h) have proven to be the best candidates to catalytically convert JP-10 into a more sensitive hydrocarbon mixture. Both catalysts are capable of converting over 90 % of JP-10 into other hydrocarbon products; however, each catalyst has its own advantages and disadvantages depending on certain reaction parameters. For instance, to achieve the lowest CRs, SAPO-5B would be advantageous at higher temperatures and nZSM-5(24h) would be advantageous at lower temperature applications.

In this study, coking is more beneficial than detrimental. First, coke production is an exothermic process, which would provide an additional source of heat. Second, coke can act as a stabilizer for the free-radicals formed during hydrocarbon cracking by providing hydrogen atoms[27]. Although, coke is the most prominent factor in catalyst deactivation, coke poisoning is not a major concern in this study due to the projected short flight times in missile applications. Coke only becomes a major concern when it affects the CR. The average CR drastically decreased from the first test with nZSM-5(24h) to its second test, suggesting the stabilizing theory to be true (see section 2.6). However, the SAPOs seem to behave on the contrary. SAPO-5A and SAPO-11 both showed an increase of CR (over double in the case of SAPO-11) in their second tests from their first. This behaviour can most likely be linked to the difference in acidity between the SAPOs and the zeolites. Zeolites have a stronger acidity, rendering them more prone to secondary reactions. Therefore, by having a few coke deposits, the amount of acidic sites are reduced, leaving less opportunity for secondary reactions.

71

The reduction in activity seen with the SAPOs suggests that they are less tolerant to coking.

Enhancing the detonability of JP-10 is just one step in developing a practical PDE system. Judging from the success with nZSM-5(24h) and SAPO-5, it will be possible to add a small chemical reactor to a fuel injection system in a missile to produce a more detonable mixture from the common, stable jet-fuel JP-10. Finding the best candidate to crack this very stable jet fuel is only the first part of this extensive study. The catalytic reaction must first be optimized by finding the best reaction parameters that will produce the best selectivity for C_2 to C_4 olefins.

References

[1] Piton, D., Yvart, P., and Serre, L. "Liquid Fueled Pulse Detonation Engines for Long-Range UAV's". pp. 387–394. AIAA 3314, 2000.

[2] Katz, A. and Davis, M. E. "Molecular Imprinting of Bulk, Microporous Silica". *Nature*, volume 403, pp. 286–289, 2000.

[3] Curran, E. and Murphy, S. *Scramjet Propulsion: Progress in Astronautics and Aeronautics*, volume 189, pp. 757–820. A. Inst. of Aeronautics and Astronautics Inc., Virginia, 2000.

[4] Spadaccini, L., Sobel, D., and Huang, H. "Deposit Formation and Mitigation in Aircraft Fuels". *J. Eng. for Gas Turbines and Power*, volume 123, pp. 741–746, 2001.

[5] Bratkovich, T., Aarnio, M., Williams, J., and Bussing, T. "Chemical Aspects of the Autoignition of Hydrocarbon-Air Mixtures". *A. Inst. of Aeronautics and Astronautics, Inc.*, pp. 1–10, 1997.

[6] Bussing, T. and Pappas, G. "An Introduction to Pulse Detonation Engines". AIAA 0263, 1994.

[7] Eidelman, S. and McLean, V. "Pulse Detonation Engine: A Status Review and Technology Development Road Map". AIAA 1997-2740.

[8] Dean, A. "Recent Developments in Approaches to Pulse Detonation Propulsion". AIAA 2003-4510, 2003.

[9] Povinelli, L. and Yungster, S. "Real Gas Effects on the Performance of Hydrocarbon-Fueled Pulse Detonation Engines". pp. 387–394. AIAA 2003-0712.

[10] Striebech, R. and Lawrence, J. "Thermal Decomposition of High-Energy Density Materials at High Pressure and Temperature". *J. Anal. Appl. Pyrolysis*, volume 00, pp. 1–14, 2002.

[11] Hitch, B. "The Effect of Autoignition-Promoting Additives on Deflagration-to-Detonation". AIAA 3719, 2002.

[12] Williams, F., Hanson, R., and Segal, C. "Fundamental Investigations of Pulse-Detonation Phenomena". In "JANNAF", pp. 151–161. CPIA Publications, 1999.

[13] Lee, J. *On the Universal Role of Turbulence in the Propogation of Deflagration and Detonation,* Computational Fluid Dynamics and reacting Gas Flow, volume 189. Springer-Verlag, 2nd edition, 1985.

[14] Romano, M., Radulescu, M., Higgins, A., and Lee, J. "Sensitization of Pentane-Oxygen Mixtures to DDT via Cool Flame Oxidation". *Comb. and Flame*, volume 132, pp. 387–394, 2003.

[15] Sidhu, S., Graham, J., and Kirk, D. "Investigation of the Effect of Additive on Ignition Characteristics of Jet Fuels: JP-7 and JP-8". *22nd Int. Symposium on Shock Waves, Imperial College, London, UK*, , no. 3810, pp. 285–289, 1999.

[16] Mikolaitis, D. W., Segal, C., and Chandy, A. "Ignition Delay for Jet Propellant 10/Air and Jet Propellant 10/High-Energy Density Fuel/Air Mixtures". *J. Prop. and Power*, volume 19, pp. 601–606, 2003.

[17] Pinard, P., Higgins, A., and Lee, J. "The Effects of NO_2 Addition on Deflagration-to-Detonation". *Comb. and Flame*, volume 136, pp. 146–154, 2004.

[18] Shtsholkin, K. and Sokolik, A. "Detonation in Gas mixtures". *Acta Physicochimica U.R.S.S.*, , no. 4, pp. 589–596, 1938.

[19] Landry, D., Grand, C., and Higgins, A. "Effects of Peroxide Additives on the Detonation Sensitivity of Hydrocarbon Fuels". AIAA 5203, 2003.

[20] Hickey, M., Ciccarelli, G., Gardiner, D., and Bardon, M. "The Reduction of Detonation Run-up Distance Using A Multi-point Ignition System". CI/CS Spring Tech. Meeting, U. of Windsor, Canada, May 2002.

[21] de Witt, B., Ciccarelli, G., Zhang, F., and Murray, S. "Detonation Initiation Studies For Pulse Detonation Engines". CI/CS Spring Tech. Meeting, U. of Windsor, Canada, May 2002.

[22] Austin, J. and Shepherd, J. "Detonations in Hydrocarbon Fuel Blends". *Comb. and Flame*, volume 132, pp. 73–90, 2003.

[23] Schauer, F., Stutrud, J., and Bradley, R. "Detonation Initiation Studies and Performance Results for Pulse Detonation Engines". AIAA 3707, 2001.

[24] Brabbs, T. and Merrit, S. "Fuel Rich Catalytic Combustion of High Density Fuel". Technical Report 3281, 1993. NASA Technical Paper.

[25] Kesten, A., Vranos, A., and Proscia, W. "Method and Apparatus to Enhance Combustion Rates and Extend Extinction Limits in High Speed Propulsion Units". 7 March 1995. US Patent 5,394,685.

[26] WordIQ.com. "Ramjet". *Wikipedia*, 2004.

[27] Gates, B., Katzer, J., and Schuit, G. *Chemistry of Catalytic Processes*. McGraw-Hill Book Company, New York, USA, 2nd edition, 1979.

[28] Cooper, M. and Shepherd, J. "Experiments Studying Thermal Cracking, Catalytic Cracking, and Premixed Partial Oxidation of JP-10". AIAA 2003-4687.

[29] Corma, A. and Orchillés, L. "Current Views on the Mechanism of Catalytic Cracking". *Micropor. Mesopor. Mater.*, volume 35.

[30] Sweetman, B. "SCRAM!" *Popular Science*, pp. 67–73, November 2002.

[31] Li, S., Varatharajan, B., and Williams, F. "Chemistry of JP-10 Ignition". *AIAA*, volume 39, no. 12, pp. 2351–2356, 2001.

[32] Davidson, D., Horning, D., Oehlschlaeger, M., and Hanson, R. "The Decomposition Products of JP-10". AIAA 3707, 2001.

[33] Green, R., Nakra, S., and Anderson, S. "Breakdown Behaviour of Fuels for Pulse Detonation Engines". Chem. Dep., U. of Utah N00014-01-0-541, 2001. Work Performed under ONR contract.

[34] Kitson, F., Larsen, B., and McEwen, C. *Gas Chromatography and Mass Spectrometry: A Practical Guide*. Academic Press, San Diego, 1996.

[35] Littlewood, A. *Gas Chromatography*. Academic Press, New York, 2nd edition, 1970.

[36] Grieken, R. V., Sotelo, J., Merendez, J., and Melero, J. "Anomalous Crystallization Mechanism in the Synthesis of Nanocrystalline ZSM-5". *Micropor. Mesopor. Mater.*, volume 39, pp. 135–147, 2000.

[37] Trong-On, D., Lutic, D., and Kaliaguine, S. "An Example of Mesostructured Zeolitic Material: UL-TS-1". *Micropor. Mesopor. Mater.*, volume 44–45, pp. 435–444, 2001.

[38] Trong-On, D. and Kaliaguine, S. "Large-Pore Mesoporous Materials with Semi-Crystalline Zeolitic Frameworks". *Angew. Chem. Int. Ed.*, volume 40, no. 17, pp. 3248–3251, 2001.

[39] Serrano, D., Aguado, J., Escola, J., and Rodríguez, J. "Nanocrystalline ZSM-5: a highly active catalyst for polyolefin feedstock recycling". *Stud. Surf. Sci. and Catalysis*, volume 142, pp. 77–84, 2002.

[40] Fernandes, G., Fernandes, V., and Araujo, A. "Catalytic Degradation of Polyethylene Over SAPO-37 Molecular Sieve". *Catalysis Today*, volume 75, pp. 233–238, 2002.

[41] López, C., Rodríguez, K., Méndez, B., Montes, A., and Machado, F. "Influence of the Silicon Content Upon the Acidity and Catalytic Properties of AFI-like Catalysts". *Appl. Catal. A*, volume 197, pp. 131–139, 2000.

[42] Zahedi-Niaki, M. H. "The synthesis, characterization and catalytic properties of titanium and vanadium aluminophosphate molecular sieves". *PhD Thesis, Laval University*, 1999.

[43] Klug, H. and Alexander, L. *X-ray Diffraction Procedures*, pp. 687–690. John Wiley & Sons, Inc. New York, 1954.

[44] S. Brunauer, E., P.H. Emmett. *J. Am. Chem. Soc.*, volume 309, no. 60, 1938.

[45] Karge, H. and Niessen, W. "Characterization by IR Spectroscopy". *Catalysis Today*, volume 8, p. 451, 1991.

[46] Young, D. and Davis, M. "IZA Synthesis Commision: SAPO-5". *Zeolites*, volume 11, p. 277, 1991.

[47] Szostak, R., Duncan, B., Aiello, R., Nastro, A., Vinje, K., and Lillerud, K. P. "IZA Synthesis Commision: AlPO4-11". *Synthesis of Micropor. Mat.*, pp. 240–247, 1992.

[48] Treacy, M., Higgins, J., and von Ballmoos, R. *Collection of Simulated XRD Powder Patterns for Zeolites*. Elsevier, 3rd edition, 1997.

[49] Zahedi-Niaki, M., Zaidi, S., and Kaliaguine, S. "Acid Properties of Titanium Aluminophosphate Molecular Sieves". *Micropor. Mesopor. Mater.*, volume 32, pp. 251–255, 1999.

[50] Scanion, J. and Willis, D. "Calculation of Flame Ionization Detector Relative Response Factors Using the Effective Carbon Number Concept". volume 23, 1985.

[51] Dietz, W. "Response Factors for Gas Chromatographic Analyses". *J. Gas Chrom.*, volume 5, pp. 68–71, February 1967.

[52] Baerlocher, C. and McCusker, L. "Verified Syntheses of Zeolitic Materials". *Stud. Surf. Sci. and Catalysis*, volume 85, p. 391, 1994.

[53] Sinha, A. and Seelan, S. "Characterization of SAPO-11 and SAPO-31 synthesized from aqueous and non-aqueous media". *Appl. Catal. A*, volume 270, pp. 245–252, 2004.

[54] Ali, M., Brisdon, B., and Thomas, W. "Synthesis, characterization and catalytic activity of ZSM-5 zeolites having variable silicon-to-aluminum ratios". *Appl. Catal. A*, volume 252, pp. 149–162, 2003.

[55] Concepción, P., López, N., Mifsud, J., and Pérez-Pariente, J. *Appl. Catal. A*, volume 151, p. 373, 1997.

[56] Wang, L., Guo, C., Yan, S., Huang, X., and Li, Q. "High-Silica SAPO-5 with Preferred Orientation: Synthesis, Characterization and Catalytic Applications". *Micropor. Mesopor. Mater.*, volume 64, pp. 63–68, 2003.

[57] Murthy, K., Kulkarni, S., and Masthan, S. K. "Sorption Properties of Modified Silicoaluminophosphate(SAPO)-5 and SAPO-11 Molecular Sieves". *Micro. Mesopor. Mat.*, volume 43, pp. 201–209, 2001.

[58] Tynjälä, P. and Pakkanen, T. "Acidic Properties of ZSM-5 zeolite modified with Ba^{2+}, Al^{3+} and La^{2+} ion-exchange". *J. Molec. Catal. A*, volume 110, pp. 153–161, 1996.

[59] Jacobs, W., Demuth, D., Schunk, S., and Schüth, F. "Sorption, sorption kinetics and diffusion of pyridine in zeolites". *Micropor. Mesopor. Mat.*, volume 10, pp. 95–109, 1997.